# POLITECNICO DI TORINO

Master's Degree in Sustainable Nuclear Energy


Master's Degree Thesis

# Monte Carlo simulation of patient organ doses in interventional radiology procedures

Supervisors

Prof. Fabio SUBBA

Prof. Maria Amor DUCH

Prof. Anna Camp BRUNES

Candidate

Andrea PERRI

2024-2025

# Acknowledgements

"Happiness can be found even in the darkest of times, if one only remembers to turn on the light." This quote from Albus Dumbledore encapsulates a message of hope, strength, and resilience that has guided me throughout this challenging academic journey. A path filled with obstacles, victories, setbacks, and moments of growth, where the light was not always easy to see but was always present, ready to shine when someone reminded me how to turn it on. It is not easy to put into words what this journey has meant to me, nor the impact that certain extraordinary and rare individuals have had along the way. There is no need to name them, for they know. They know who they are, they know how they illuminated my steps when darkness seemed overwhelming. With quiet gestures or powerful words, they helped me rediscover the strength within me, even when I doubted it myself. To these individuals, who, like lighthouses in the storm, showed me the way without ever forcing the helm, I owe my deepest gratitude. There is no achievement in this work that does not reflect the light they have shared. There is no success I have reached that is not also a testament to their trust, patience, and love. Thank you to those who believed in me on the days I couldn't believe in myself, to those who celebrated my small milestones as if they were great triumphs, and to those who, with a smile or a kind word, reminded me that every obstacle is just a step toward something greater. This accomplishment is not mine alone: it is the result of every lesson imparted, every encouragement offered, and every hand that turned on the light when all seemed dark. And there is no need for explicit thanks—**they know**.

“La luce la si può trovare anche negli attimi più bui, se solo uno si ricorda di accendere la luce.” Questa frase di Albus Silente racchiude in sé un messaggio di speranza, forza e resilienza che mi ha accompagnato durante questo intenso viaggio accademico. Un percorso fatto di sfide, conquiste, cadute e momenti di crescita, in cui la luce non è sempre stata facile da vedere, ma è sempre esistita, pronta a brillare quando qualcuno mi ricordava come accenderla. Non è facile tradurre in parole il significato che questo percorso ha avuto per me, né l’impatto che alcune persone, straordinarie e rare, hanno avuto lungo la strada. Non serve nominarle, perché loro sanno. Sanno chi sono, sanno quanto hanno illuminato i miei passi quando l’oscurità sembrava prevalere. Con gesti silenziosi o parole potenti, mi hanno aiutato a riscoprire la forza che avevo dentro, anche quando io stesso ne dubitavo. A queste persone, che, come fari nella tempesta, mi hanno indicato la direzione senza mai forzare il timone, va il mio ringraziamento più profondo. Non c’è risultato in questo lavoro che non porti il riflesso della loro luce. Non c’è successo raggiunto che non sia anche merito della fiducia, della pazienza e dell’amore che mi hanno donato. Grazie a chi ha saputo credere in me nei giorni in cui io non ci riuscivo, a chi ha gioito dei miei piccoli traguardi come fossero grandi conquiste, e a chi, con un sorriso o una parola, mi ha ricordato che ogni ostacolo è solo un passaggio verso qualcosa di più grande. Questo traguardo non è soltanto mio: è il frutto di ogni insegnamento ricevuto, di ogni incoraggiamento offerto, di ogni mano che ha saputo accendere la luce quando tutto sembrava buio. E non c’è bisogno di fare ringraziamenti espliciti, **loro lo sanno**.

# Table of Contents

# List of Tables

# List of Figures

# Summary

Medical procedures using ionising radiation constitute by far the largest contribution to people by man-made radiation sources. Although the benefit for the patients exposed will normally outweigh the risk associated with the radiation, tissue reactions have been reported for patients undergoing fluoroscopically guided procedures (Balter et al, 2010). In this context, WG12 of the European Radiation Dosimetry Group EURADOS (a network of 80 European institutions and more than 600 members) carries out research projects and coordinated activities within the field of area dosimetry. A specific task group (https://eurados.sckcen.be/en/working-groups/wg12-dosimetry-medical-imaging/wg12-task- groupsanchor-wg12-sg2-patient-dosimetry) was set up to estimate organ doses in interventional radiology. The main purpose is to characterize the variability of measurements and calculations depending on the different parameters that can affect the dose reconstruction (DICOM RDSR data, manufacturers, dosimetry tools, ...). Results of different Monte Carlo codes (MCNP6, MCNPX, GATE/Geant4, PHITS, PyMCGPU-IR) will be compared in several test cases. Among the 20 participants, UPC's research group is already participating with the dose calculation by using PyMCGPU-IR. This master thesis will allow to also participate with PENELOPE/penEasy.

# Chapter 1

# Radiological protection

## 1.1 Biological effects of ionising radiations

The radiological protection is the discipline which aim consist in studying and preventing harms deriving from ionising radiations. These radiations are able to modify the structure of atoms and molecules inside our tissues, leading to have very severe consequences. The ionising radiation may have two different action on the DNA molecule:

- Direct action
- Indirect action

The first one consist in a direct interaction between the ionising radiation and the DNA, instead the second one consists in the interaction, always of the ionising radiation, with others components in the cell, mainly with water molecules. The problem of the indirect actions is that they lead to produce free radicals. In fact the ionising radiation, interacting with the molecules of water can create the Hydroxyl radical which is very reactive and is one of the main responsible of the damages to the mammalian cells. These interactions, as already mentioned, can damage the DNA, in particular we can highlight two cases among the possible injuries to DNA:

1. The radiations break one strand of the DNA
2. The radiations break both of the strands of the DNA

In the first scenario we have two possible situations, the first one consists in the reparation of the DNA using some enzymes which repair the broken strand using the healthy part of the strand. This lead to have a new strand completely identical to the previous one, but sometimes this reparation lead to have some mutations in the DNA. In the second case instead, the DNA can be no more able to repair

itself so the interaction of the ionising radiation with the DNA can lead to cell killing. Once a huge number of cells die, the tissues can lose their capability to perform their function, in this situation we talk about deterministic effects or tissue reactions. These effects usually occur right after, or shortly after, the irradiation. The deterministic effects are dose sensitive as shown in the picture.

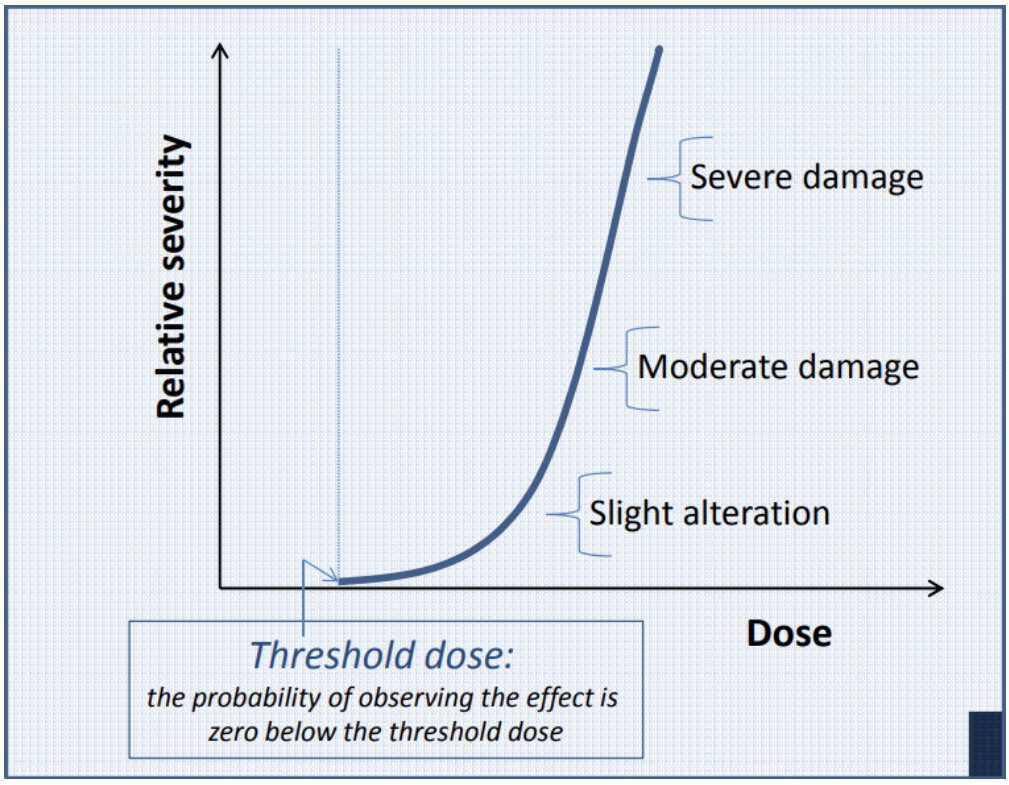


**Figure 1.1:** Graph of severity of deterministic effects as function of the dose received

As illustrated by the figure, below a certain value of the dose we do not have deterministic effects consequences, but beyond this threshold value the severity of the effects increase , almost in an exponential way, with the dose. On the other hand we have the stochastic effects. These effects come from the mutations of the DNA of the cells. The severity of them is not dose dependent but the likelihood with which they occur it is.

In Table 1.1 some results are presented that highlight the deterministic skin damage following exposure to radiation. The results emphasize the severity of the skin reaction, as evaluated by the NCI (National Cancer Institute) Skin Reaction Grade, and its progression over time.

| Band | Single-Site Acute Skin-Dose Range (Gy)* | NCI Skin Reaction Grade | Prompt | Early | Midterm | Longterm |
|---|---|---|---|---|---|---|
| A1 | 0-2 | NA | No observable effecs expected | No observable effects expected | No observable effects expected | No observable effects expected |
| A2 | 2-5 | 1 | Transient erythema | Epilation | Recovery from hair loss | No observable effect expected |
| B | 5-10 | 1-2 | Transient erythema | Erythema,epilation | Recovery; at higher doses prolonged erythema, permenet partial epilation | Recovery; at higher doses, dermal atrophy or induration |
| C | 10-15 | 2-3 | Transient erythema | Erythema,epilation; possible dry or moist desquamation; recovery from desquamation | Prolonged erythema, permanent epilation | Telangiectasia; dermal atrophy or induration; skin likely to be weak |
| D | >15 | 3-4 | Transient erythema; after very high doses, edema and acute ulceration; long-term surgical intervention likely to be required | Erythema, epilation; moist desquamation | Dermal atrophy; secondary ulceration due to failure of moist desquamation to heal; surgical intervention likely to be required; at higher doses, dermal necrosis,surgical intervention likely to be required | Telangiectasia;dermal atrophy or induration; possible late skin breakdown; wound might be persistent and progress into a deeper lesion; surgical intervention likely to be required |

**Table 1.1:** Tissue Reactions from Single-Delivery Radiation Dose to Skin of the Neck, Torso, Pelvis, Buttocks, or Arms ( Prompt $<$ 2 weeks; early, 2–8 weeks; midterm, 6–52 weeks; long term $>$ 40 weeks) [1]

As can be observed from the figures 1.2 and 1.3, the possible effects of radiation can cause very serious damage, in this case to the skin, which, if not treated with care and appropriate caution, can lead to permanent consequences for the patient that may hinder their daily life. Therefore, the study and analysis of the dose delivered to patients as a result of therapies involving the use of radiation is of significant interest.

**Figure 1.2:** NCI skin toxicity grade 2.Radiation injury due to overlapping radiation fields in 80-year-old woman [1]

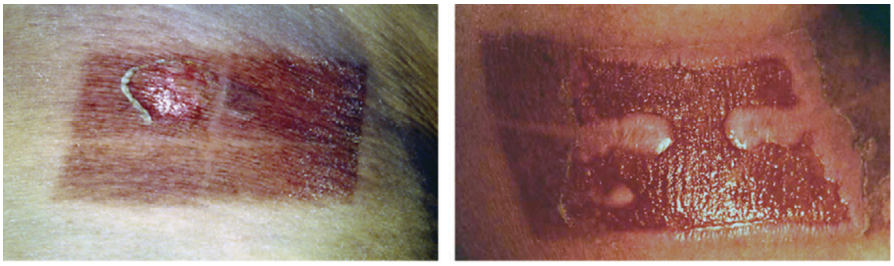

**Figure 1.3:** Early erythema and developing moist desquamation in a diabetic woman caused by a localization radiographic exposure[1]

## 1.2 Quantities used radiological protection

During the years, in order to develop models and study more in details the effects of ionising particles in the matter, have been developed some quantities. Among them we are going to explain:

- Fluence
- Energy fluence
- KERMA
- Absorbed dose
- Mean absorbed dose
- Equivalent dose
- Effective dose
- KAP: Kerma Area Product

### 1.2.1 Fluence

The fluence is a radiometric quantity which defines the number of particles, indicated as N, which cross an infinitesimal sphere centered at point $\vec{r}$ and with cross sectional area d**A**. So the fluence in this point is defined as [2]:

$$\phi(\vec{r}) = \frac{dN}{dA} \tag{1.1}$$

The unit of measure of the fluence are [$m^{-2}$].

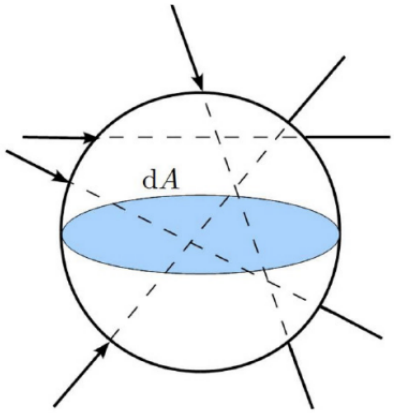


**Figure 1.4:** Geometrical representation of the fluence

### 1.2.2 Energy fluence

The energy fluence represents the energy carried by the particles through the centered sphere in $\vec{r}$ with cross sectional area d**A**. Indeed if we call with **R** the radiant energy, that is the energy carried by the particles, the energy fluence is defined as [2]:

$$\psi(\vec{r}) = \frac{dR}{dA} \tag{1.2}$$

The unit of measure of the energy fluence are [J/m$^{-2}$].

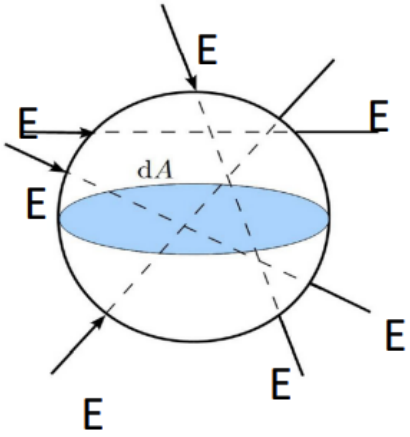


**Figure 1.5:** Geometrical representation of the energy fluence

### 1.2.3 KERMA

The KERMA, which acronym means "Kinetic Energy Released per unit Mass", is a dosimetric quantity only defined for interactions due to uncharged particles, like photons or neutrons, and represents the energy transferred by these particles to charged particles as results of their interaction. The mathematical formulation for KERMA is [2]:

$$d\epsilon_{\mathbf{tr}} = (R_{\text{in}})_{\text{u}} - (R_{\text{out}})_{\text{u}}^{\text{nonr}} + \sum \text{Q} \tag{1.3}$$

Where:

- $d\epsilon_{\text{tr}}$ represents the energy transferred to the small volume dV
- $(R_{\text{in}})_{\text{u}}$ is the energy of uncharged particles entering the volume dV
- $(R_{\text{out}})_{\text{u}}^{\text{nonr}}$ is the energy of uncharged particles who leaves the volume dV, this term does not count the radiative losses
- $\sum \text{Q}$ takes into account the energy derived from the rest mass, in particular if we have phenomena who transform mass in to energy it assumes positive values and negative values if the contrary

The unit of measure of KERMA are gray [Gy], in particular 1 Gy is equal to 1 J $kg^{-1}$

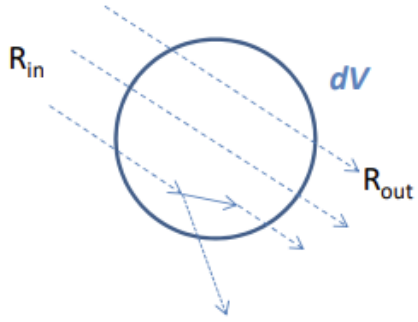


**Figure 1.6:** Geometrical representation of the KERMA

### 1.2.4 Absorbed dose

The asorbed dose is another dosimetric quantitity, it defines the energy imparted by the particles, charged and uncharged, per unit mass. Indeed, the absorbed dose is defined for all kind of ionising radiations. The formula to evaluate it is the following one [2]:

$$\bar{\epsilon} = (R_{\text{in}})_{\text{u}} + (R_{\text{in}})_{\text{c}} - (R_{\text{out}})_{\text{u}} - (R_{\text{out}})_{\text{c}} + \sum \text{Q} \tag{1.4}$$

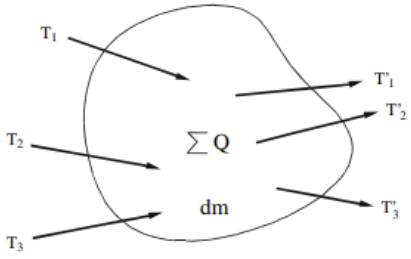


**Figure 1.7:** Geometrical representation of the absorbed dose

In this formula the only two new terms are:

- $(R_{\text{in}})_{\text{c}}$ is the radiant energy of charged particles entering dV
- $(R_{\text{out}})_{\text{c}}$ is the radiant energy of charged particles leaving dV

Also for the absorbed dose the unit of measure is gray

### 1.2.5 Mean absorbed dose in a tissue or organ

The mean absorbed dose represents the absorbed dose received by a particular organ or tissue. Its unit of measure is still gray, and the mathematical formulation is [2]:

$$\overline{D_{\text{T}}} = \frac{\int D(x,y,z)\rho(x,y,z)\,dV}{\int \rho(x,y,z)\,dV}$$

The integral is performed over the whole volume of the tissue and it considers also the local density to take into account the heterogeneity of the organ or tissue of interest.

### 1.2.6 Organ equivalent dose

The equivalent dose, also called biological dose [3] represents the absorbed dose in a specific tissue or organs weighted by the so called weighting factor [3], indeed it is expressed as the product between the absorbed dose and the radiation $w_R$ [2]:

$$H_T = \sum_R w_R D_{T,R} \tag{1.6}$$

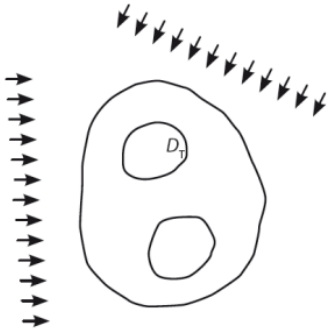


**Figure 1.8:** Geometrical representation of the absorbed dose

The units of the equivalent dose are sievert [Sv] [3]. The already mentioned radiation weighting factor is a parameter who allows us to distinguish the influence of the different particles, this derive by the fact that not all the particles produce the same biological effects, see table 1.2.

| Type and energy range | Radiation weighting factors $w_R$ |
|---|---|
| Photons, all energies | 1 |
| Electrons and muons | 1 |
| Protons and charged pions | 2 |
| Alpha particles, fission fragments, heavy ions | 20 |
| Neutrons | Continuos function of neutron energy |

**Table 1.2:** Radiation weighting factors for different types and energy ranges [2]

### 1.2.7 Effective dose

The effective dose is a quantity used to take into account that not every organs or tissue have the same response to the radiations, some will be more sensitive than others and so the probability for diseases or damages related to the radiations will be higher. The units are still the sievert and the effective dose is calculated summing all the equivalent dose multiplied by the corresponding tissue weighting factor [2]:

$$E = \sum_T w_T \sum_R w_R D_{T,R} = \sum_T w_T H_T \tag{1.7}$$

$$\sum_T w_{\mathbf{T}} = 1 \tag{1.8}$$

| Organ/Tissue | Number of tissues | $w_T$ | Total contributions |
|---|---|---|---|
| Lung, stomach, colon, bone morrow, breast, remainder | 6 | 0.12 | 0.72 |
| Gonads | 1 | 0.08 | 0.08 |
| Thyroid, oesophagus, bladder, liver | 4 | 0.04 | 0.16 |
| Bone surface, skin, brain, salivary glands | 4 | 0.01 | 0.04 |

**Table 1.3:** Tissue weighting factors in the 2007 Reccomendations [2]

### 1.2.8 KAP: Kerma Area Product

KAP is a measure of the energy imparted to air by ionizing radiation over entire physical area of the X-ray field. It is the appropriate measurement for total radiation incident on the patient's skin and is an indication for the total amount of radiation imparted during the examination [4]. The kerma area product is obtained by evaluating the air kerma and multypling it by the xray beam cross-sectional area, the final unit of measurement is Gy $\cdot cm^2$[5]

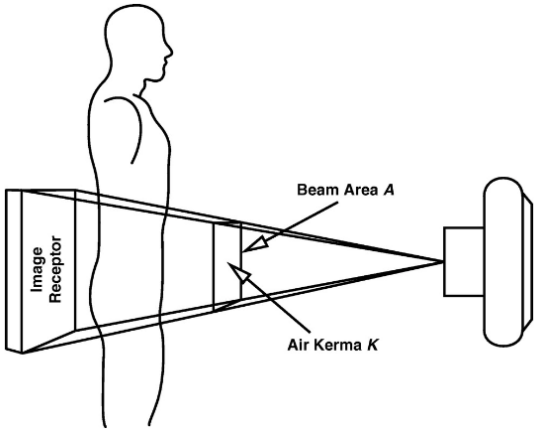


**Figure 1.9:** Schematic representation of KAP evaluation [5]

# Chapter 2

# Fluoroscopically guided interventional procedures

The use of X-rays has become an integral part of our daily lives, especially in the field of medicine. In Europe, hundreds of millions of X-ray exams are performed every year. These radiological exams are not only used to diagnose fractures or skeletal injuries, but they also encompass a wide range of procedures, such as dental X-rays, computed tomography (CT), and fluorography. On average, each European citizen undergoes about 1.1 X-ray exams annually, demonstrating how widespread and accessible these tools are [6]. As show in 2.1, the majority of procedures that use x-rays belong to the plain radiography, which consists into producing images by passing x-rays through the internal structure and recording the shadow cost by these structures, in the plain radiography they are also included the dental procedures, which represent a big fraction of the total radriographies. By Top 20 it means the 20 types of examination or procedure that were consistently found to be amongst the highest contributors to the collective effective dose [7].

| Country | Plain radiography | Fluoroscopy | Computed tomography | Interventional radiology | Overall total frequency per 1000 population |
|---|---|---|---|---|---|
| AT | 1160,3 | 46,7 | **98,0** | **7,8** | 1313 |
| BE | 1098,9 | 32,4 | 185,3 | 37,1 | 1354 |
| BG | **434,2** | **40,5** | **36,4** | **2,3** | **513** |
| CH | **1533,0** | **19,9** | **101,0** | **13,2** | **1667** |
| CY | 729,5 | 22,1 | 107,8 | 6,2 | 866 |
| CZ | 901,9 | 29,7 | 78,8 | 5,4 | **1016** |
| DE | **1247,9** | **45,7** | **131,9** | **11,1** | **1437** |
| DK | 465,2 | 17,0 | **94,7** | 3,1 | **580** |
| EE | 809,2 | 22,7 | 161,5 | 4,4 | 998 |
| EL | **608,5** | **28,1** | **93,8** | **3,8** | **734** |
| ES | 1435,7 | 24,7 | 100,2 | 4,2 | 1565 |
| FI | **1119,8** | **10,2** | **61,1** | **5,6** | **1197** |
| FR | **1002,6** | **20,2** | **118,7** | 6,9 | 1148 |
| HR | 701,2 | 46,8 | 48,7 | 7,1 | 804 |
| HU | 1691,8 | 55,8 | 110,0 | 6,2 | 1864 |
| IE | 1218,5 | 20,3 | 66,8 | 13,0 | 1319 |
| IS | **1956,8** | **20,1** | **147,2** | **5,1** | **2129** |
| IT | 1034,3 | 31,5 | 131,1 | 8,0 | 1205 |
| LT | 941,6 | 70,9 | 56,4 | 12,5 | **1081** |
| LU | 915,1 | 21,0 | 188,6 | 2,9 | 1128 |
| LV | **1104,3** | **30,7** | **116,4** | **3,7** | **1255** |
| MD | 610,5 | 34,6 | 9,4 | 0,3 | 655 |
| ME | 723,3 | 17,4 | 106,5 | 2,7 | 850 |
| MK | 572,8 | 27,3 | 20,3 | 5,0 | 625 |
| MT | 638,9 | 52,4 | 58,4 | 6,4 | 756 |
| NL | 603,9 | 18,1 | 73,5 | 5,3 | 701 |
| NO | 728,2 | 21,9 | 150,5 | 8,2 | 909 |
| PL | 1091,9 | 18,0 | 49,3 | 5,9 | 1165 |
| PT | 1398,9 | 15,4 | 158,0 | 3,8 | 1576 |
| RO | **227,9** | **41,1** | **27,5** | **0,2** | **297** |
| RS | **666,7** | **53,3** | **66,7** | **2,0** | **789** |
| SE | 647,0 | 24,3 | 94,2 | 5,3 | 771 |
| SI | 903,0 | 14,9 | 52,7 | 6,1 | 977 |
| SK | 1232,6 | 18,0 | 69,3 | 3,8 | 1324 |
| UA | 1181,2 | 28,1 | 8,0 | 0,4 | 1218 |
| UK | **668,2** | **17,5** | **55,4** | **5,1** | **746** |

**Figure 2.1:** The overall total frequencies of x-ray procedures per 1000 population for all countries and for the main groups (plain radiography, fluoroscopy, computed tomography and interventional radiology). Plain radiography includes dental procedures. Real numbers (not estimated from Top 20) are in bold. [6]

| **Exam type or category** | **% of total frequency*** | **% of total S*** |
|---|---|---|
| ***Plain film radiography*** | | |
| 1. Chest/thorax | 12 - 29 | 0.7 – 5.2 |
| 2. Cervical spine | 2.0 – 5.4 | 0.05 – 2.3 |
| 3. Thoracic spine | 1.0 – 3.1 | 0.5 – 3.7 |
| 4. Lumbar spine (inc. LSJ) | 2.8 – 9.6 | 2.0 - 17 |
| 5. Mammography | 0.3 – 15 | 0.6 – 4.7 |
| 6. Abdomen | 1.1 – 4.3 | 1.1 – 4.7 |
| 7. Pelvis & hip | 6.3 – 10 | 2.8 – 9.4 |
| ***Radiography/Fluoroscopy*** | | |
| 8. Ba meal | 0.3 – 0.9 | 0.8 – 5.9 |
| 9. Ba enema | 0.1 – 2.0 | 0.5 - 13 |
| 10. Ba follow | 0.05 – 0.3 | 0.2 – 1.6 |
| 11. IVU | 0.3 – 2.0 | 1.2 – 8.7 |
| 12. Cardiac angiography | 0.2 – 1.3 | 1.0 – 9.9 |
| *All angiography* | *1.1 – 2.4* | *6.4 - 16* |
| ***CT*** | | |
| 13. CT head | 1.8 – 5.4 | 3.0 – 7.9 |
| 14. CT neck | 0.06 – 0.9 | 0.1 – 1.1 |
| 15. CT chest | 0.5 – 1.5 | 6.1 - 12 |
| 16. CT spine | 0.3 – 2.8 | 1.5 - 13 |
| 17. CT abdomen | 0.01 – 3.0 | 1.9 - 26 |
| 18. CT pelvis | 0.03 – 1.5 | 0.3 – 9.7 |
| 19. CT trunk | 0.1 – 5.6 | 1.1 - 27 |
| *All CT* | *4.5 – 15* | *28 - 59* |
| ***Interventional*** | | |
| 20. PTCA | 0.1 – 0.3 | 0.5 – 3.6 |
| *All interventional* | *0.2 – 1.3* | *3.5 - 14* |
| **TOTAL 1-20** | **50-70** | **70-90** |

**Figure 2.2:** List of the Top 20 procedures [7]

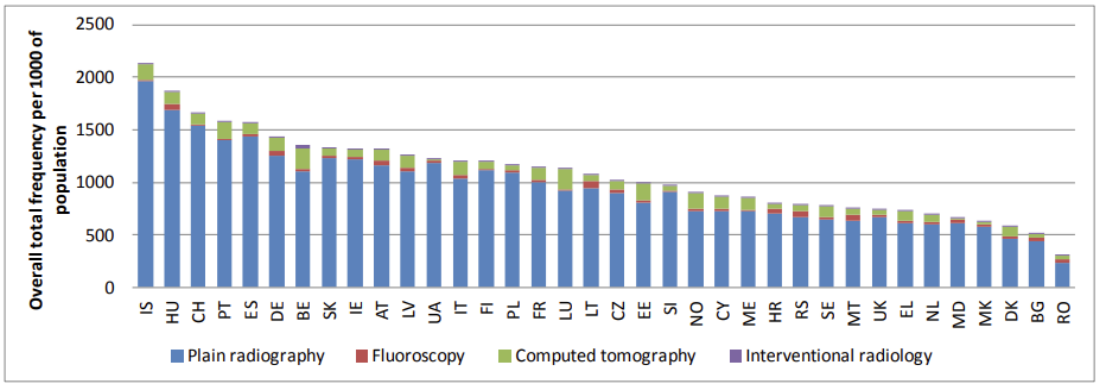


**Figure 2.3:** Overall total frequencies per 1000 of population for different countries. The relative contributions of the four main groups (plain radiography including dental, fluoroscopy, computed tomography and interventional radiology) are also shown. Plain radiography includes dental procedures. [6]

## 2.1 What fluoroscopically guided interventional procedures are

Fluoroscopically guided interventional procedure use X-rays to guide small instruments such as catheters through blood vessels or other pathways in the body [8]. These procedures can be diagnostic and therapeutic and result in a reduced risk to the patient than conventional surgery. As already mentioned, this method uses X-rays to produce images with a rate of 25-30 images per second, although the radiation dose for each individual image is very low, the cumulative dose can sometimes result in high organ dose, particularly high skin doses[9]. Regarding the fluoroscopy, there are two main aspects to take into account, since it uses radiations we have to manage the risks of:

1. The most exposed skin of the patient's body, this area will be the critical target for our X-rays beam and will receive the highest value of absorbed dose [9]. This is relevant for the deterministic effects that could be occur to the patient.

2. The organ doses imparted to the patient [9], this is related to the stochastic effects.

In line with this aspects or radiological protection of the patients undergoing fluoroscopically guided procedures, the European Directive 2013/59/Euratom establishe the fundamental safety regulations for protecting against risks associated with ionising radiation. In particular, it shall be ensured that:

- the use of fluoroscopy equipment without a device to automatically control the dose rate, or without an image intensifier or equivalent device, is prohibited.
- any equipment used for interventional radilogy has a device or a feature informing the practitioner and those carrying out practical aspects of the medical procedures of quantity of radiation produced by the equipment during the procedure.
- any equipment used for interventional radiology and computed tomographyand any new equipemnt used for planning, guiding and verification purposes has a device or a feature informing the practitioner, at the end of the procedure, of relevant parameters for assessing the patient dose.


**Figure 2.4:** Interventional room for fluoroscopically guided procedure [10]

The voltage, generally used for the beams, range from 50 to 125 kVp , and the normal dose rates received by the skin goes from 1 $mGy/min$, in this case we are talking about the very-low-dose-rate fluoroscopy, to some $Gy/min$ [1]. Interventional radiology systems have incorporated automatic control exposure (ACE) systems. These kind of systems help to provide a consistent optical densitysignal-to-noise ratio between images, regardless of patient influence factors such as size and density. Therefore, medical staff do not need to manually select the best combination of kV or filtration for each image.

| Hepatic | Neuro | Biliary/ERCP | Cardiac |
|---|---|---|---|
| Philips X-Radfluoro (2001) | | Siemens Polystar(1995) | Siemens Polystar (1995)<br>Philips X-Radfluoro (2001) |
| | GE Advantx LCA | | GE Innova 2000 (2003)<br>Philips Integris 3000 |
| Toshiba Angiorex-US031A/J1 (2000) | Toshiba Angiorex-US031A/J1 (2000) | | Siemens HICOR |
| GE Advantx LCA (1995) | GE Advantx LCA (1995) | GE Advantx LCA (1995) | Philips Integris BH 3000 (1995)<br>Siemens Angiostar Plus (2000) |
| Siemens Polystar (1996) | Siemens Neurostar Biplane (2000) | GE Advantx AFM (1992)<br>Siemens Polystar (1996) | Siemens Coroscop HS (1994 to 2003)<br>Siemens Axiom Sensis Biplane (2004)<br>GE Advantx LC DC (1994) |
| Siemens Multistar Plus/TOP (1998) | Siemens Neurostar Biplane | | 2*GE Advantx LC+DLX (2000)<br>Siemens Bicor Plus/TOP (1998)<br>Philips Integris H3000 (1997) |

**Table 2.1:** Some commercially available interventional radiology machines[11]

Another important parameter to take into account is the distance between the patient and the X-rays source. This distance is called source-to-skin distance, also denoted with the acronym (SSD) or focus-to-skin distance (FSD) [12]. This distance should be kept as large as possible, in order to minimize the dose received by the patient. Indeed, since the intensity of the photon beam decreases with the square of the distance, for higher distances the dose imparted by the X-rays will be lower. Different story for what regard the distance between the source and the panel detector which produces the image. This distance is called source to image receptor distance (SID) [12]. This distance must be as low as possible to reduce

the time necessary to obtain the images.

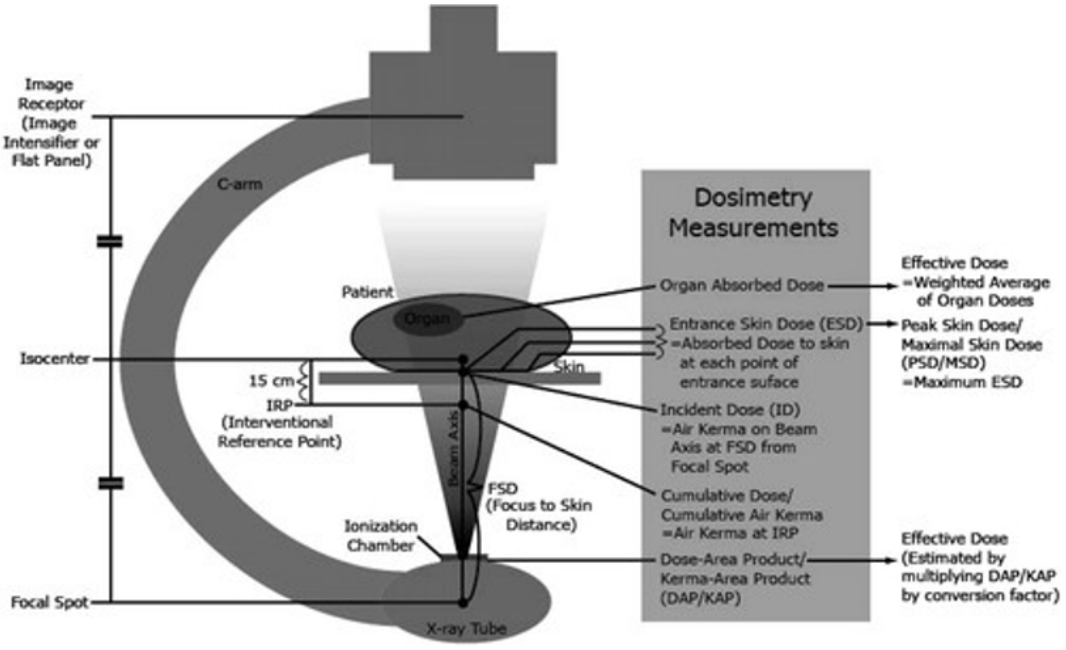


**Figure 2.5:** Schematic layout of the fluoroscopically guided procedure room[13]

Figure 2.2 shows the schematic layout of a typical isocentric machine used for interventional radiology. As indicated in this figure, the KAP is usually measured by means of a transmission ionisation chamber (nearly radiotransparent) placed between the X-ray tube and the patient. Subsequently, the air kerma at the interventional reference point (15 cm below the isocenter) is calculated. Organ and effective doses can be calculated through KAP. Other important aspects, that technicians must take into account during the fluoroscopically procedure, are [12]:

- Try to keep unnecessary body parts away from the beam
- Try to use a pulsed fluoroscopy at low pulsed rate.
- Try to collimate as much as possible the X-rays beam, in this way the beam will interact only with the area of interest and not with other regions.
- Try to minimize the time of the procedure.
- Monitoring the patient dose.

## 2.2 Interaction of photons with matter

The photons were discovered when Albert Einstein studied the photoelectric effect, a phenomenon in which a light of a single frequency hits a metallic surface. It was observed that some electrons were emitted by this metallic surface for certain values of the frequency. Einstein, in order to explain the results, demonstrated that light must be quantized, and the energy carried by the light itself was due to elementary particles, named photons which carry a well defined value of energy. The photons energy is equal to [14]:

$$E = hf \tag{2.1}$$

Where:

- $h$ is the Planck's constant, the value of it is $h = 6.626 \times 10^{-34}\,\mathrm{J\,s}$
- $f$ is the frequency of the light, its unit of measure is $\mathrm{s}^{-1}$

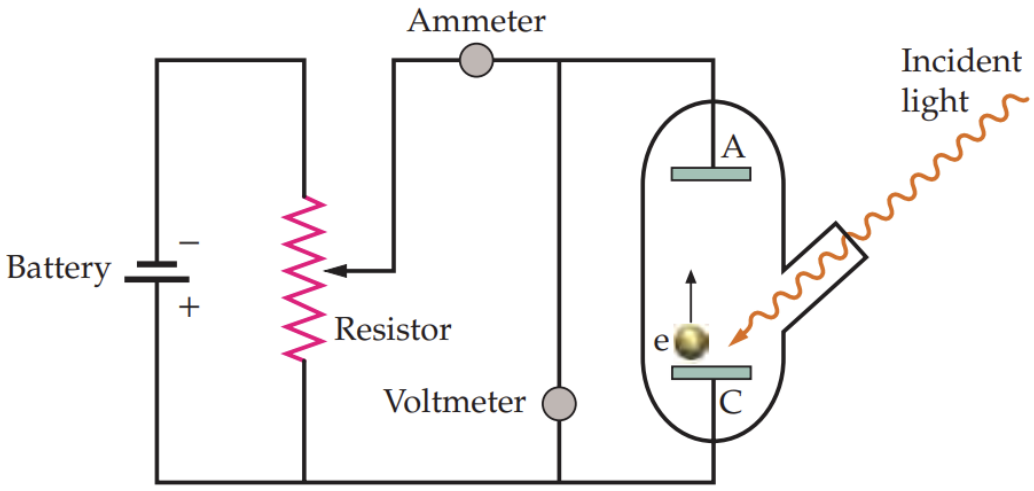


**Figure 2.6:** Experimental setup for the photoelectric effect [14]

After, during the years, the physics started studying these particles and their interactions with the matter. The interactions of photons with matter is well defined by the so called cross section $\sigma$ , which is a geometrical representation of the interaction of photons with the matter. Indeed it can be interpreted as the area of interaction between a photon and an atom of the matter. The cross section $\sigma$ is defined as:

$$\sigma = \pi r_0^2 \tag{2.2}$$

The unit of measure are $cm^2$ , and $r_0$ represent the impact parameter, if the photons will travel at a distance greater than $r_0$ from the atom it will not undergo any kind of reactions. Another important parameter used to study the interaction of photons with matter is the attenuation coefficient $\mu$, this parameter can be viewed as the probability per unit length to undergo reactions with atoms in the matter, is obtained starting by the cross section definition. Indeed the attenuation coefficient is defined as:

$$\mu = \sigma n_T \tag{2.3}$$

The term $n_T$ represents the atomic density of the material, its unit of measure are $cm^{-3}$ so the final unit of measure of the attenuation coefficient is $cm^{-1}$. Of course these parameters, $\sigma$ and $\mu$, are not constant but depend by:

- Energy of the photons
- Type of reaction
- Material of the target

Thanks to this parameter we can derive a very easy equation to see how the photons behave in the matter. For the sake of the simplicity we are going to make the following assumptions:

1. Monocromatic and monoenergetic photon beam
2. Target's thickness of length $L$
3. Initial photon beam intensity equal to $I_0$
4. No secondary collisions or reactions
5. 1-D geometry along $x$

Under these assumptions we want to evaluate how the photons intensity change with the length travelled by the photons themselves, in few words we are going to write the difference among the photon intensity between $x$ and $x + dx$ . So using the definition of $\mu$ we can write:

$$I(x + dx) - I(x) = -I(x)\mu dx \tag{2.4}$$

Rearranging the terms we obtain:

$$\frac{I(x + dx) - I(x)}{dx} = -I(x)\mu \tag{2.5}$$

The right term assumes a negative value because when photons travel in the matter the can interact with others atoms so more they travel in the matter more with more probability they will interact. Looking at the first term, it is nothing less than the derivative of the photon beam intensity with respect the length, in this case along x. So we can rewrite the equation in the following way:

$$\frac{dI(x)}{dx} = -I(x)\mu \tag{2.6}$$

This is a simple ordinary differential equation that can be solved using the method of separable variables, and using the Cauchy's theorem [15], we are able to obtain the unique solution thanks to the initial condition of the photon beam intensity $I_0$:

$$I(x) = I_0 e^{-\mu x} \tag{2.7}$$

This equation says that the intensity of the photon beam decreases exponentially with the increasing of the path length travelled by the photons. The photons can undergo different types of reactions, in particular they can produce the following interactions [16]:

- Photoelectric effect
- Coherent (Rayleigh) scattering
- Incoherent (Compton) scattering
- Electron-positron pair production

The photoelectric effect consists in an atom who absorbs an incident photon, this lead the atom to get in an excited state. This energy is used by an electron to escape by its quantum orbital state, and if the energy of the photon is high enough the electron can also leave the atom itself, leading to have some emission of fluorescence. The Rayleigh scattering consists in an interaction during which the photons is scattered by the external electrons of the atom without excitation of it [16], in the Compton scattering a photon interact with an orbital electron which absorbs it and emits a second photon with different energy [16]. The last interaction is the electron-positron pair production, this interaction occurs when the photon is absorbed close to a nucleus or an electron, this reaction leads to have a production of an electron and a positron and it has a threshold energy to happen which is of $2m_e c^2$ [16].

Each interaction has its own cross section $\sigma$ , and has a different trend in the energy spectrum. Usually the reactions are studied using the mass attenuation

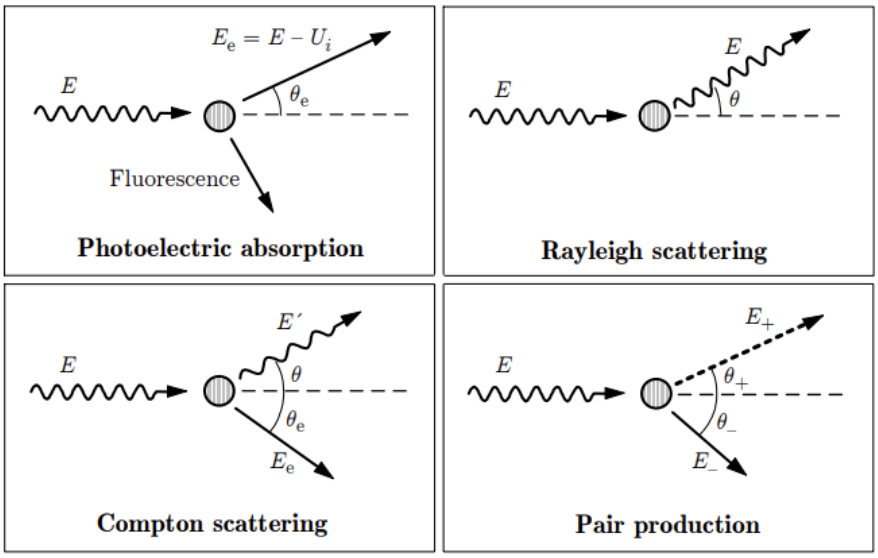


**Figure 2.7:** Photons reactions in the matter [16]

coefficient, which is defined as the ration of the attenuation coefficient over the density of the material:

$$\frac{\mu}{\rho} = \frac{N_A}{A_M}\sigma \tag{2.8}$$

The unit of measure of this quantity are $cm^2/g$, in the formula $N_A$ is the Avogadro's number and $A_M$ is the molecular weight of the matter. This value will be different from interaction to interaction, since the cross sections are not all the same. If we want to define the total mass attenuation coefficient we need to consider all the $\sigma$ of the different reactions, so [16]:

$$\left(\frac{\mu}{\rho}\right)_{\text{tot}} = \frac{N_A}{A_M}(\sigma_{R_a} + \sigma_{C_o} + \sigma_{P_h} + \sigma_{P_p}) \tag{2.9}$$

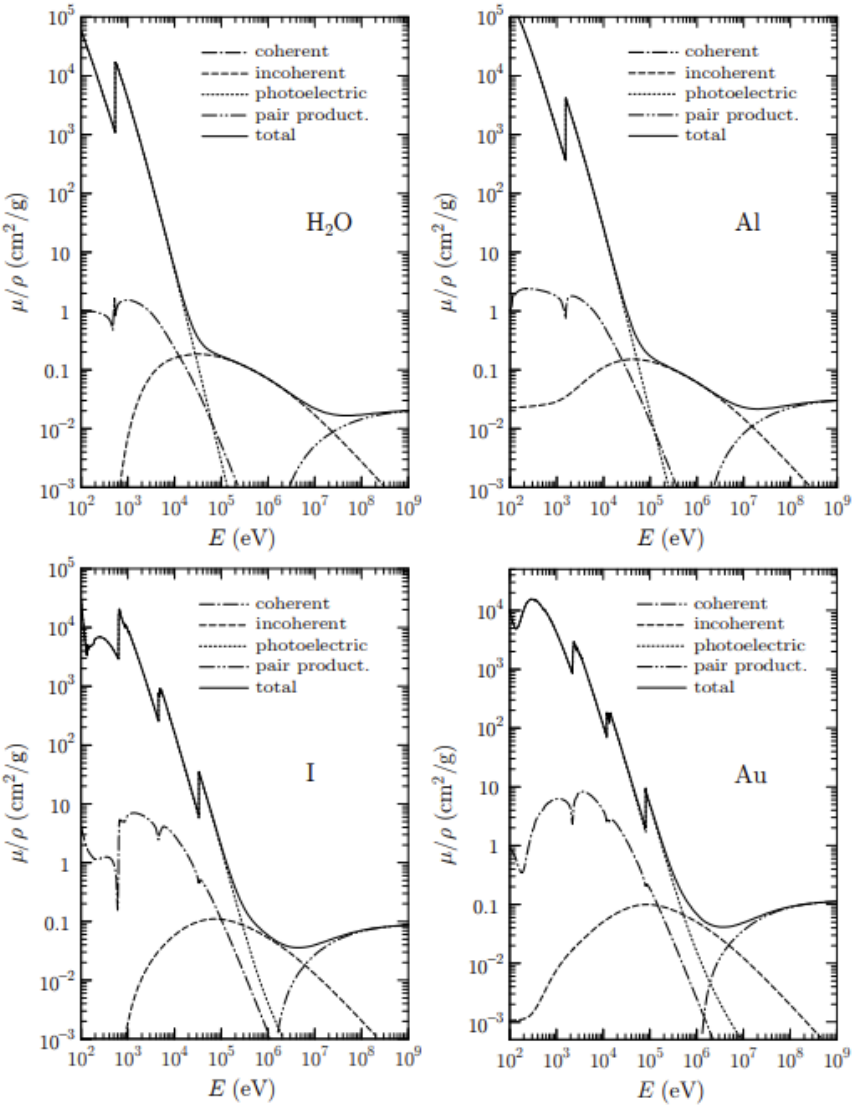


**Figure 2.8:** Mass attenuation coefficient of different element for different energy values [16]

## 2.3 X-ray tubes

The discovery of X-rays was made by the German scientist Wilhelm Roentgen in 1895. This discovery revolutionized not only physics but also medicine, as an application of X-rays in the medical field was quickly found. In fact, by 1896, the first cancer treatment using X-rays was recorded [17]. X-rays are produced through X-ray tubes. These instruments remain largely unchanged from the original design

developed by the same German scientist.

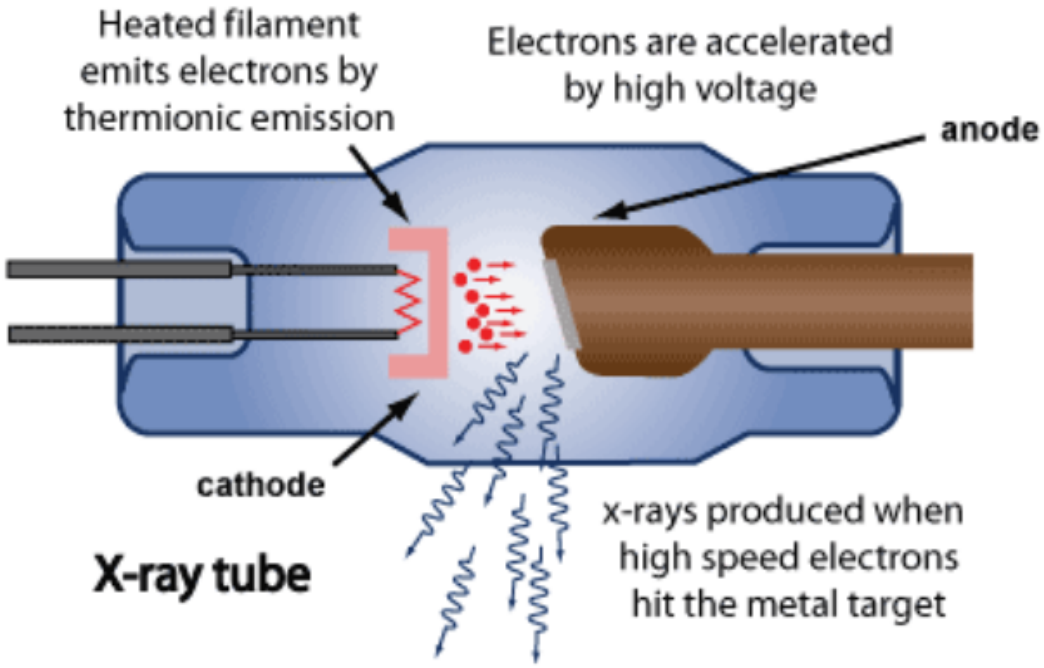


**Figure 2.9:** Schematic configuration for a X-ray tube [18]

As shown in the figure, an X-ray tube consists of a tube in which a vacuum is created. Inside this tube, there is an anode and a cathode with a potential difference applied between them. Inside the tube there can be one or two filaments, depending if different focal-spot sizes are needed, and it is from these filaments that electrons are released through the thermionic effect. The thermionic effect consists of the emission of electrons due to high thermal energy [19]. The elevated temperatures of the heated filaments provide the outer orbital electrons with enough energy to escape from their orbitals. The emitted electrons are then accelerated by the applied potential and directed toward the anode. This anode is generally made of materials with a high atomic number Z. In this way, the electrons are rapidly decelerated, emitting X-rays due to the Bremsstrahlung effect. The Bremmstrahlung's effect consists into emission of electromagnetic radiation as consequences of the deceleration of electrons or charged particles due to an electric field, this electric field could be the one generated by other charged particles or nuclei [20]. In X-ray tubes, the energy spectrum reaches its maximum energy level, equal to the maximum value of the applied potential. The applied potential plays

a crucial role in determining the energy of the emitted rays; for example, rays generated at 20-150 kVp are typically used in the diagnostic field primarily for imaging purposes, while rays with higher energy levels are generally employed for superficial treatments[17].

# Chapter 3

# PENELOPE/penEasy

## 3.1 PENELOPE/penEasy code

Penelope is a set of Monte Carlo codes, written using Fortran language, which solve the transport of elementary particles like photons, electrons and positrons. This code is released by different agencies, in particular by the OECD Nuclear Energy Agency Data Bank and by the Radiation Safety Information Computational Center of the Oak Ridge National Laboratory[21]. The OECD is an organisation, created on 1 February 1958. The goal of OECD was to create a community in which to expose new discoveries and solutions in the nuclear field, thus giving all member countries the opportunity to have safe nuclear energy and above all to use the latter for peaceful purposes. The member countries are: Australia, Austria, Belgium, Canada, Chile, the Czech Republic, Denmark, Estonia, Finland, France, Germany, Greece, Hungary, Iceland, Ireland, Israel, Italy, Japan, Korea, Latvia, Lithuania, Luxembourg, Mexico, the Netherlands, New Zealand, Norway, Poland, Portugal, the Slovak Republic, Slovenia, Spain, Sweden, Switzerland, Turkey, the United Kingdom and the United States [16]. The code is able to run Monte Carlo simulation in basically every kind of materials and the energy range goes from few hundred eV to 1 GeV [16]. The code uses the random number generator called RANECU, and in particular the programs uses the function RAND, which provides 32-bit floating-point numbers that are uniformly distributed in the interval between 0 and 1. PenEasy instead, is a program which provides users the possibility to set different source models, tallies and other parameters. All the input informations must be provided through several input text files, these files contain information about:

- Number of histories, run time...
- Source models

- Geometry of the problem
- Tallies, which are basically the quantities the user wants to evaluate

### 3.1.1 PENGEOM package

Inside PENELOPE code there is PENGEOM, which is a Fortran package which manage the interface crossing of particles. Basically the strategy adopted is the following one: when a particle reaches the interface between two bodies, its tracking it is stopped and reinitialized using the new material's properties. With PENGEOM it is possible to define almost every material as a body delimited by quadric surfaces or by using voxels, both the concepts of quadric surface and voxels will be explained in the next subsections. The geometry of the problem must be defined in a specific input file with the extension `.geo`. This package allows to create a hierarchic structure between bodies. In fact, we think of a bodies as an objects, these object can be grouped together module, this reduce significantly the computational cost of the simulation. Since the visualization of geometries defined byy quadric surfaces is not easy, in the code there are two visualization programs which display the geometry defined in the input file, in particular these two programs are:

- GVIEW2D: this program displays the two-dimensional geometry
- GVIEW3D: this program makes the same but displaying the three-dimensional geometry

### 3.1.2 Quadric surfaces

As already mentioned before, with PENELOPE code it is possible to describe objects as bodies delimited by quadric surfaces. Let consider the generic surfaces described by the function $F(\vec{r})$ , this function is assumed to be continuos and differentiable [16] in the three dimensional space. This surface cut the domain in two parts characterized by the sign of $F(\vec{r})$ , the sign is called surface side pointer, this parameter is crucial in the geometry definition, depending by its value that can be +1 or -1 the inner or outer region is selected. Then a point $\vec{r_0}$ is considered to be inside the surface if $F(\vec{r_0}) < 0$ , otherwise is considered outside. The surfaces used are called quadric because they are expressed by analytical implicit equation of the second order. The general equation of a quadric surface is:

$$F(\vec{r}) = A_{xx}x^2 + A_{xy}xy + A_{xz}xz + A_{yy}y^2 + A_{yz}yz + A_{zz}z^2 + A_x x + A_y y + A_z z + A_0 = 0 \tag{3.1}$$

Usually the previous equation is expressed using the matrix notation, so the equation can be written as:

$$F(\vec{r}) = r^T B r + A^T r + A_0 = 0 \tag{3.2}$$

Where:

- r = $\begin{bmatrix} x \\ y \\ z \end{bmatrix}$
- A = $\begin{bmatrix} A_x \\ A_y \\ A_z \end{bmatrix}$
- B = $\begin{bmatrix} A_{xx} & \frac{1}{2}A_{xy} & \frac{1}{2}A_{xz} \\ \frac{1}{2}A_{xy} & A_{yy} & \frac{1}{2}A_{yz} \\ \frac{1}{2}A_{xz} & \frac{1}{2}A_{yz} & A_{zz} \end{bmatrix}$

For the sake of the simplicity, in PENELOPE code is it possible to define surfaces using reduced quadric surfaces. Starting from the general surfaces just described, some translations and rotations are applied. This lead us to decrease the number of parameters that describe the surface. The result is a reduced quadric surface defined by the following expression:

$$F_r(\vec{r}) = I_1 x^2 + I_2 y^2 + I_3 z^2 + I_4 z + I_5 = 0 \tag{3.3}$$

The different indices assume the value -1 and +1, and depending by the combination of the indices it is possible to define different surfaces, each one with a simmetry with respect the z-axis.

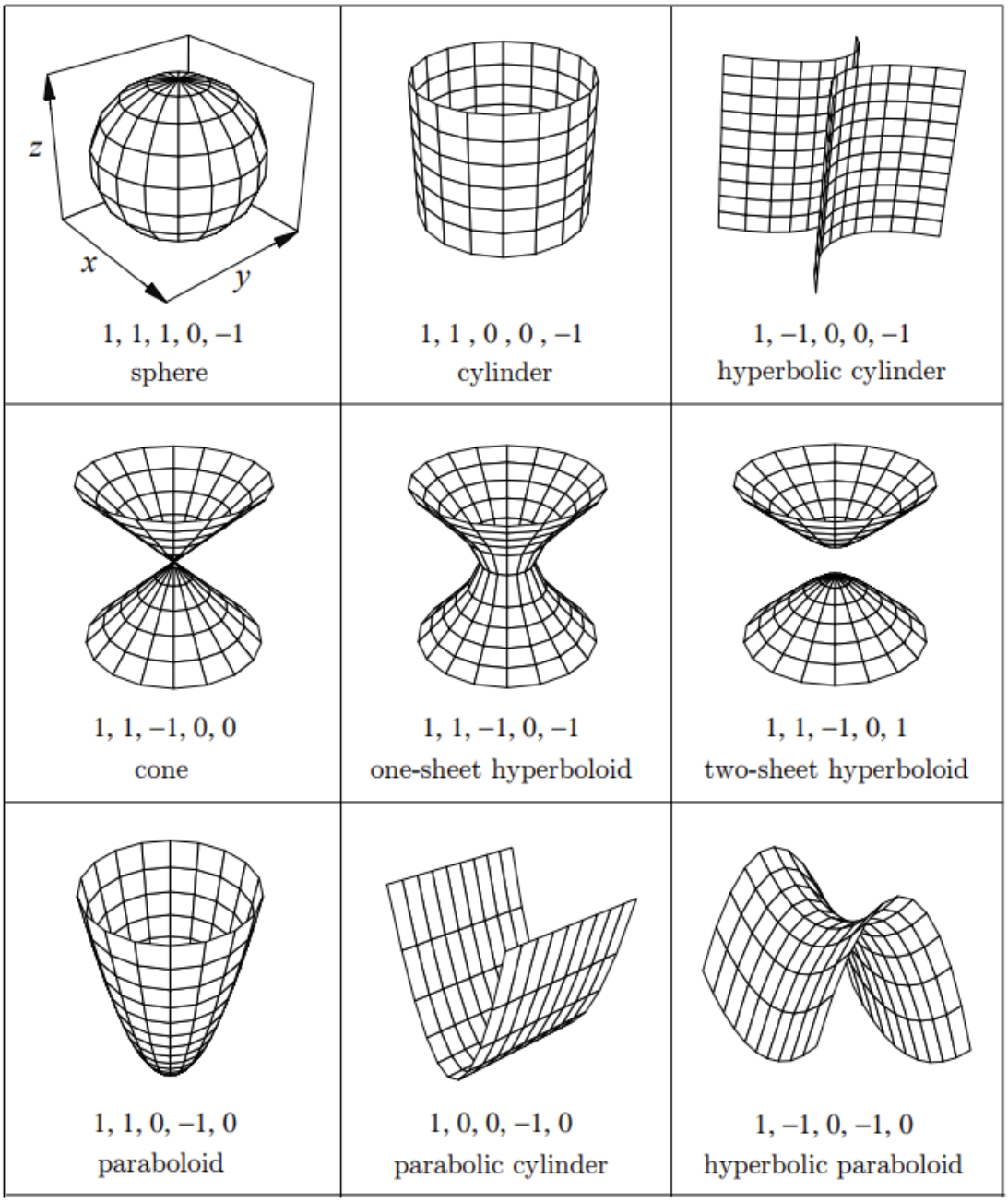


**Figure 3.1:** Reduced quadric surfaces with their indices[16]

As already explained before, these surfaces have a simmetry with respect the z-axis, what usually happens it that these surfaces must be rotated to represent the correct layout of the problem. In order to perform the rotations of the quadric

surfaces PENELOPE uses a set of Euler angles [16], that are $\omega$, $\theta$ and $\phi$. These angles can assume respectively the values the following values:

- $\omega \in (0,2\pi)$
- $\theta \in (0,\pi)$
- $\phi \in (0,2\pi)$

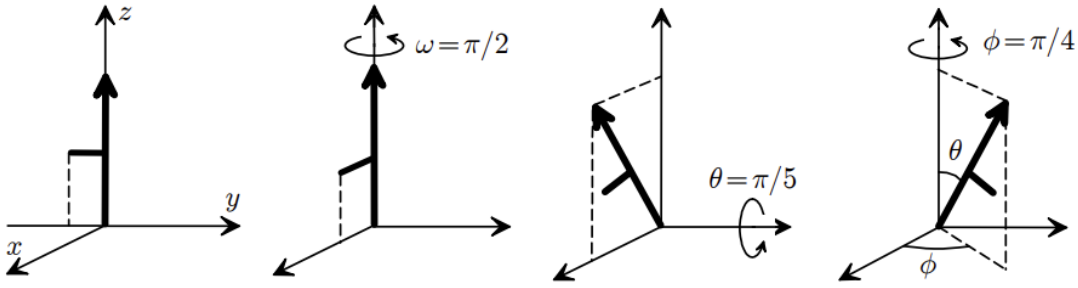


**Figure 3.2:** Euler angles[16]

As can be seen by the figure above, both $\omega$ and $\phi$ angle perform a rotation along the z-axis instead $\theta$ performs a rotation along the y-axis. All the rotations are described by proper rotation matrices that are:

$$R(\phi\vec{z}) = \begin{bmatrix} \cos\phi & -\sin\phi & 0 \\ \sin\phi & \cos\phi & 0 \\ 0 & 0 & 1 \end{bmatrix} \tag{3.4}$$

$$R(\omega\vec{y}) = \begin{bmatrix} \cos\omega & -\sin\omega & 0 \\ \sin\omega & \cos\omega & 0 \\ 0 & 0 & 1 \end{bmatrix} \tag{3.5}$$

$$R(\theta\vec{z}) = \begin{bmatrix} \cos\theta & 0 & \sin\theta \\ 0 & 1 & 0 \\ -\sin\theta & 0 & \cos\theta \end{bmatrix} \tag{3.6}$$

The final rotation matrix it nothing else that the product of the three matrices described above:

$$R(\omega,\theta,\phi) = R(\phi\vec{z})R(\theta\vec{z})R(\omega\vec{z}) \tag{3.7}$$

Everything explained so far is specified and read through the input file. In this file is possible to define:

- Quadric surfaces: using both the implicit or reduced form

- Bodies: which are delimited by the surfaces and moreover they can be delimeted by other bodies or modules

- Modules: basically they are like bodies, they can contain other bodies and modules.

```
0000000000000000000000000000000000000000000000000000000000000000000000
SURFACE (  A4)   reduced form
INDICES=(I2,I2,I2,I2,I2)
X-SCALE=(        E22.15        ,  I4)              (DEFAULT=1.0)
Y-SCALE=(        E22.15        ,  I4)              (DEFAULT=1.0)
Z-SCALE=(        E22.15        ,  I4)              (DEFAULT=1.0)
  OMEGA=(        E22.15        ,  I4) DEG          (DEFAULT=0.0)
  THETA=(        E22.15        ,  I4) DEG          (DEFAULT=0.0)
    PHI=(        E22.15        ,  I4) RAD          (DEFAULT=0.0)
X-SHIFT=(        E22.15        ,  I4)              (DEFAULT=0.0)
Y-SHIFT=(        E22.15        ,  I4)              (DEFAULT=0.0)
Z-SHIFT=(        E22.15        ,  I4)              (DEFAULT=0.0)
0000000000000000000000000000000000000000000000000000000000000000000000
SURFACE (  A4)   implicit form
INDICES=( 0, 0, 0, 0, 0)
    AXX=(        E22.15        ,  I4)              (DEFAULT=0.0)
    AXY=(        E22.15        ,  I4)              (DEFAULT=0.0)
    AXZ=(        E22.15        ,  I4)              (DEFAULT=0.0)
    AYY=(        E22.15        ,  I4)              (DEFAULT=0.0)
    AYZ=(        E22.15        ,  I4)              (DEFAULT=0.0)
    AZZ=(        E22.15        ,  I4)              (DEFAULT=0.0)
     AX=(        E22.15        ,  I4)              (DEFAULT=0.0)
     AY=(        E22.15        ,  I4)              (DEFAULT=0.0)
     AZ=(        E22.15        ,  I4)              (DEFAULT=0.0)
     A0=(        E22.15        ,  I4)              (DEFAULT=0.0)
1111111111111111111111111111111111111111111111111111111111111111111111
  OMEGA=(        E22.15        ,  I4) DEG          (DEFAULT=0.0)
  THETA=(        E22.15        ,  I4) DEG          (DEFAULT=0.0)
    PHI=(        E22.15        ,  I4) RAD          (DEFAULT=0.0)
X-SHIFT=(        E22.15        ,  I4)              (DEFAULT=0.0)
Y-SHIFT=(        E22.15        ,  I4)              (DEFAULT=0.0)
Z-SHIFT=(        E22.15        ,  I4)              (DEFAULT=0.0)
0000000000000000000000000000000000000000000000000000000000000000000000
BODY    (  A4) Text describing the body ...
MATERIAL(  A4)
SURFACE (  A4), SIDE POINTER=( 1)
BODY    (  A4)
MODULE  (  A4)
0000000000000000000000000000000000000000000000000000000000000000000000
MODULE  (  A4)  Text describing the module ...
MATERIAL(  A4)
SURFACE (  A4), SIDE POINTER=( 1)
BODY    (  A4)
MODULE  (  A4)
1111111111111111111111111111111111111111111111111111111111111111111111
  OMEGA=(        E22.15        ,  I4) DEG          (DEFAULT=0.0)
  THETA=(        E22.15        ,  I4) DEG          (DEFAULT=0.0)
    PHI=(        E22.15        ,  I4) RAD          (DEFAULT=0.0)
X-SHIFT=(        E22.15        ,  I4)              (DEFAULT=0.0)
Y-SHIFT=(        E22.15        ,  I4)              (DEFAULT=0.0)
Z-SHIFT=(        E22.15        ,  I4)              (DEFAULT=0.0)
0000000000000000000000000000000000000000000000000000000000000000000000
```

**Figure 3.3:** General geometry input file[16]

### 3.1.3 Voxelised geometry

The PENELOPE/penEasy program allows to build geometries by using voxels. These voxels are rectangular or cuboid three-dimensional elements. They all have the same dimensions and they are made with homogeneous material and mass density, defined in the input geometry file. This definition for the geometry allows to build complex geometry where there are a lot of different materials involved. When creating geometry using voxels, they determine the origin of the reference system, as the origin is identified by the vertex of the first voxel defined in the geometry file. It is also possible to create geometries using both voxels and quadric surfaces, taking care to correctly select which material should be transparent relative to the voxels. This prevents overlapping of multiple materials in the same region.

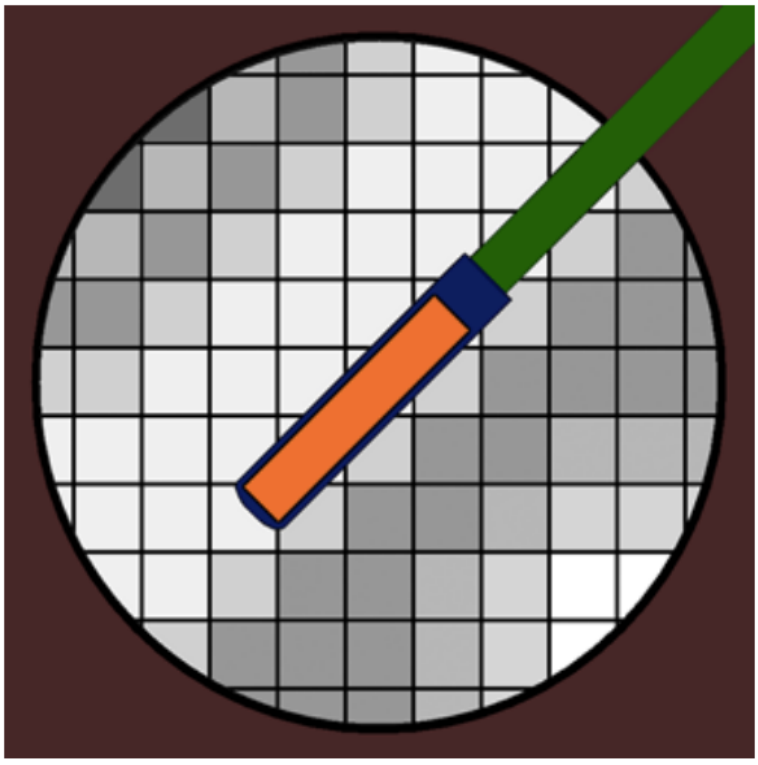

**Figure 3.4:** Example of geometry defined by using both quadric surfaces and voxels [21]

### 3.1.4 Material database

In order to run a simulation, the material's parameters must be specified. Inside PENELOPE program there is a material data file with 280 different materials, for each one there are information about physical properties, nuclear parameters like the different cross-sections, information about the energies of the atomic electron shells and so on. Moreover PENELOPE gives the possibility to define new materials inserting some parameters about the material we want to define like the mass density, stoichiometric indices or weight fraction of element inside the mixture or compound.

# Chapter 4

# Analysis of the problem

The problem in question consists in studying, from a radiological point of view, the fluoroscopically guided interventional procedure. Simulation wants to replicate, as much as possible the real setup that is present in the hospital's room where this procedure is performed. Obviously some simplifications regarding the geometry of the problem were necessary. Going into more detail, the objective of the study is to calculate and analyze some radiological quantities that come out of the result of the interaction of the photons, deriving from the therapy, with the patient's tissue for different geometry setup. Two different simulations will be performed, one using only quadric geometries to describe and define the whole geometry setup instead the second one will use a mixture between quadric geometries and voxilized geometry to define the patient.

## 4.1 Problem definition, quadric Surfaces

The geometry setup consists into a room of 8 m x 5 m x 3 m filled with air. The walls are 0.5m thick and made of concrete. The patient is assumed to be a cylinder made of PMMA (length 170 cm, diameter 30 cm). The cylinder lays on a table made of aluminum (319 cm x 50 cm) and thickness of 1.1 mm. Above the cylinder there is rectangular detector (30 cm x 40 cm x 5 cm) made of silicon.

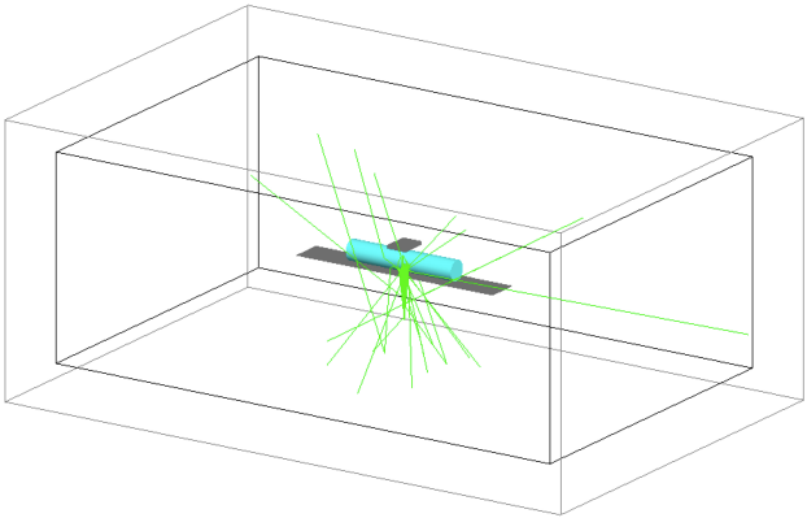

**Figure 4.1:** Schematic view of the geometry for quadric surfaces [22]

The x-ray source is assumed to do not have a tube structure, so it is treated as a simple x-ray beam. The spectrum of this source has been evaluated using SpeakCalc software, using as maximum voltage 80 kVp and an aluminium thickness of 3.5 mm with a theta angle of 30 degree. The source must be modeled such a way that below 15 cm by the isocenter the cone beam has a radius of 5 cm.

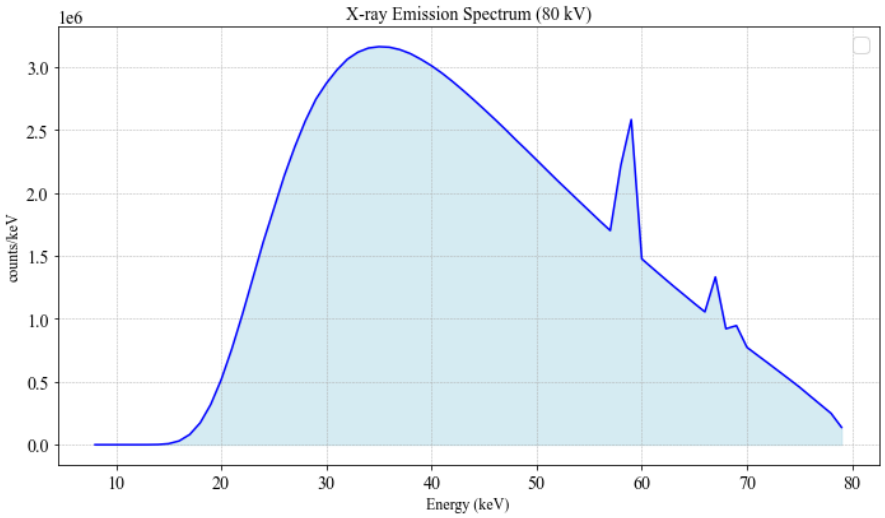


**Figure 4.2:** X-ray spectrum used for the simulation

The materials compositions, expressed by weight fraction, of the domain are:

- PMMA : d=1.195 g/cm$^3$, $n = 3$
  1. Hydrogen; f=0.0.080541
  2. Carbon; f=0.599846
  3. Oxygen; f=0.319613
- Air : d=1.29 mg/cm$^3$, $n = 4$
  1. Nitrogen; f=755269
  2. Oxygen; f=0.231781
  3. Argon; f=0.012827
  4. Carbon; f=0.000124
- Concrete : d=2.3 g/cm$^3$, $n = 10$
  1. Hydrogen; f=0.010000
  2. Carbon; f=0.001000
  3. Sodium; f=0.016000
  4. Oxygen; f=0.529107
  5. Magnesium;f=0.002000
  6. Aluminium;f=0.033872
  7. Silicon; f=0.337021
  8. Potassium;f=0.013000
  9. Calcium; f=0.044000
  10. Iron; f=0.014000
- Aluminum(100%) : d=2.75 g/cm$^3$
- Silicon(100%) : d=2.33 g/cm$^3$

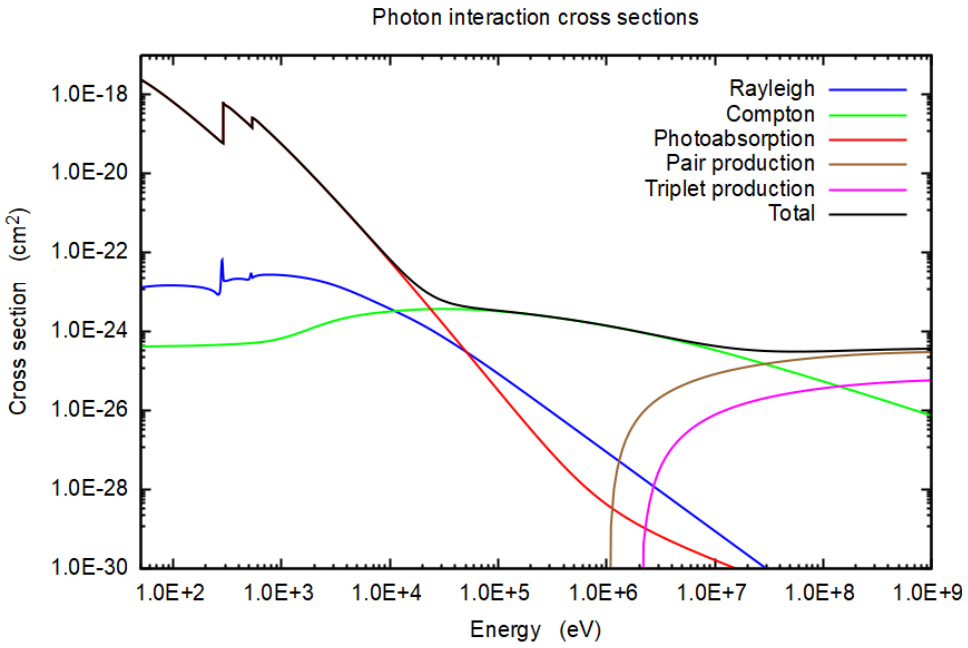


**Figure 4.3:** PMMA cross sections, taken by PENELOPE software

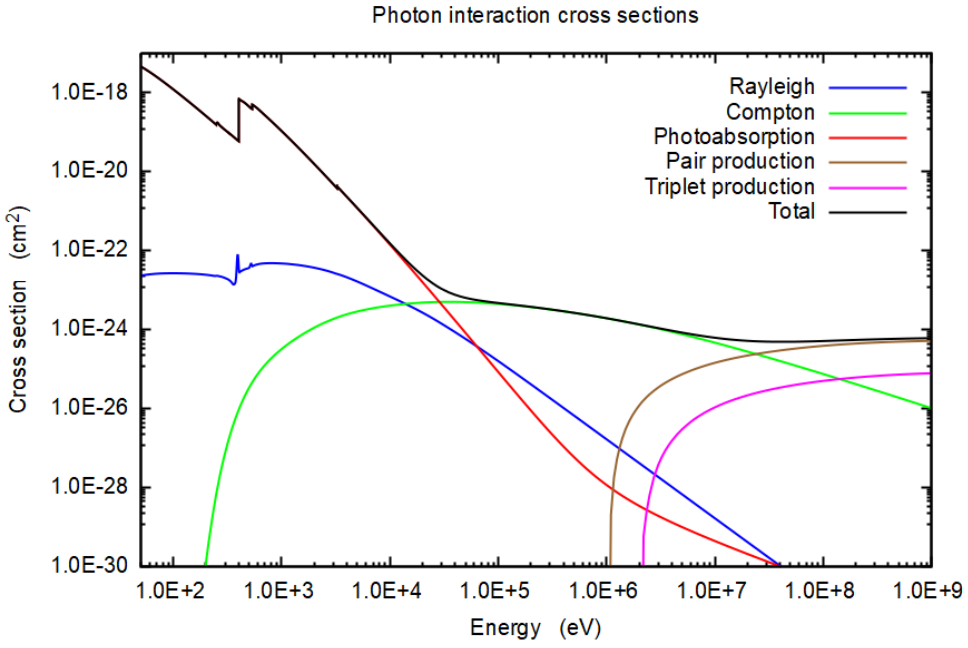


**Figure 4.4:** Air cross sections, taken by PENELOPE software

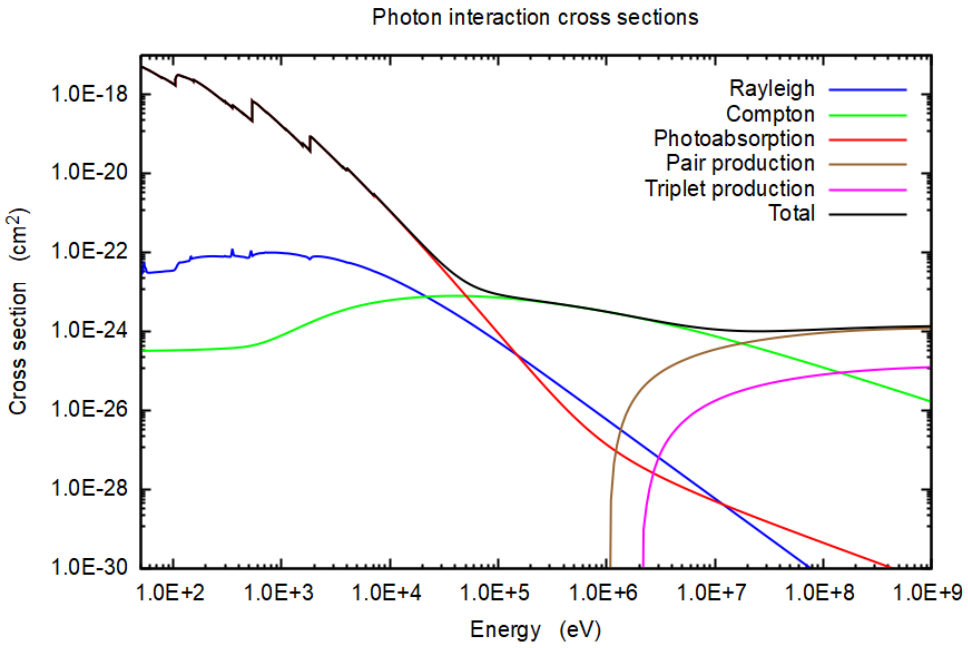


**Figure 4.5:** Concrete cross sections, taken by PENELOPE software

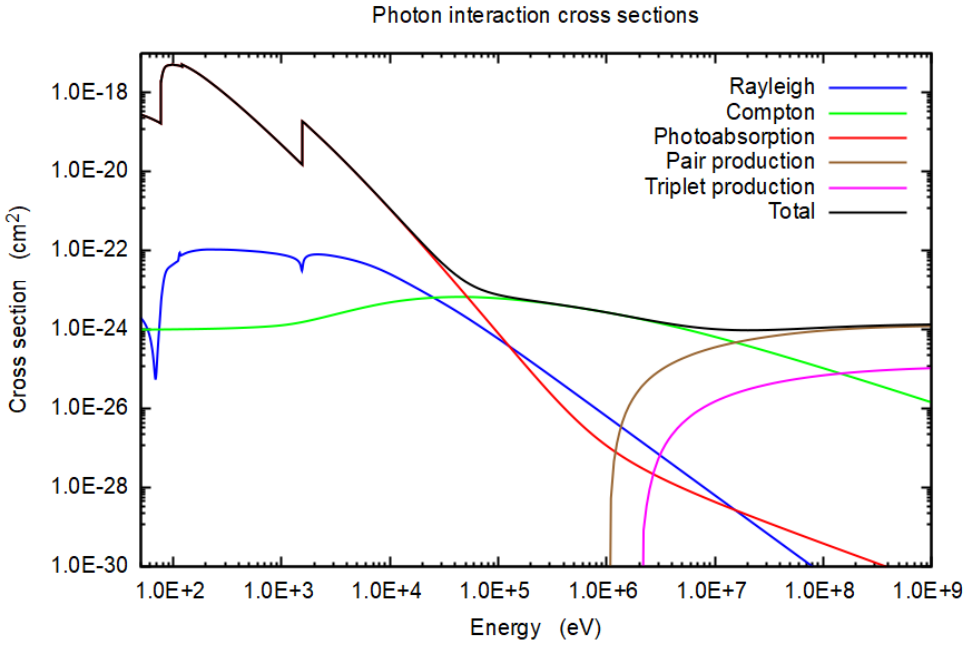


**Figure 4.6:** Aluminum cross-sections, taken by PENELOPE software

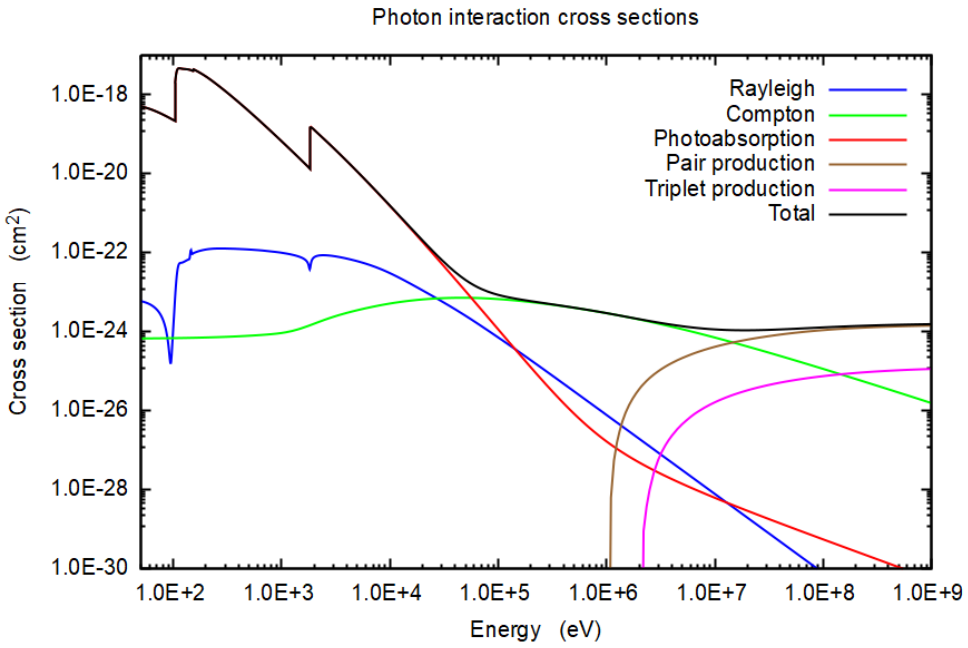


**Figure 4.7:** Silicon cross-sections, taken by PENELOPE software

Other important parameters for the simulations are the different distances (SSD, SID and SDD), already mentioned before, from the source. In the following problem the distances used to run the simulation are:

| | |
|---|---|
| SSD (Source-skin distance) | 66 cm |
| SID (Source-isocenter distance) | 81 cm |
| SDD (Source-detector distance) | 100 cm |

**Table 4.1:** Distances from the x-ray source

All the distances refer to the center of each body. In particular, the isocenter is the center of the reference system, so the one with coordinates equal to $\vec{O} = (0,0,0)$. For this case, where the whole geometry setup is defined through quadric geometries, the quantities that must be evaluated are:

1. Air kerma computed in a 1x1x1 $cm^3$ volume located 10 cm after the focal point of the source (on the beam axis)

2. X-ray energy spectrum with / without the table (computed in a 1x1x1 $cm^3$ volume located at isocenter on the beam axis)

3. Dose and fluence with / without the table (computed in a 1x1x1 $cm^3$ volume located at isocenter on the beam axis)

4. Depth dose distributions (beam axis) in the phantom for X-ray beam on the bottom (0°) and on the top (180°) of the table.

### 4.1.1 Geometry definition, Quadric Surfaces

To reproduce the geometry required for the problem under examination, a total of 37 quadric surfaces were necessary. These quadric surfaces were used to define the various elements within our geometry, such as the aluminum table, the box centered at the isocenter, the cylinder, the silicon detector, the air, and the concrete walls. An additional element was defined to accurately impose the geometry of the source at the operational point. The geometry was created using a total of 4 bodies and 3 modules.

| Surface | Value (cm) |
|---|---|
| z | +0.5 |
| z | -0.5 |
| y | +0.5 |
| y | -0.5 |
| x | +0.5 |
| x | -0.5 |

**Table 4.2:** Box in the isocenter

| Surface | Value (cm) |
|---|---|
| z | +85 |
| z | -85 |
| Cylinder | R=15 |

**Table 4.3:** Cylinder

| Surface | Value (cm) |
|---|---|
| z | -15 |
| z | -15.11 |
| y | +159.5 |
| y | -159.5 |
| x | +25 |
| x | -25 |

**Table 4.4:** Aluminum table

| Surface | Value (cm) |
|---|---|
| z | -15 |
| z | -15.11 |
| y | +5 |
| y | -5 |
| x | +5 |
| x | -5 |

**Table 4.5:** Source pointer

| Surface | Value (cm) |
|---|---|
| z | +19 |
| z | +24 |
| y | +15 |
| y | -15 |
| x | +20 |
| x | -20 |

**Table 4.6:** Detector

| Surface | Value (cm) |
|---|---|
| z | +150 |
| z | -150 |
| y | +400 |
| y | -400 |
| x | +250 |
| x | -250 |

**Table 4.7:** Air in the room

| Surface | Value (cm) |
|---|---|
| z | +200 |
| z | -200 |
| y | +450 |
| y | -450 |
| x | +300 |
| x | -300 |

**Table 4.8:** Concrete walls

The final geometry, created through quadric surfaces is showed in the next pictures.

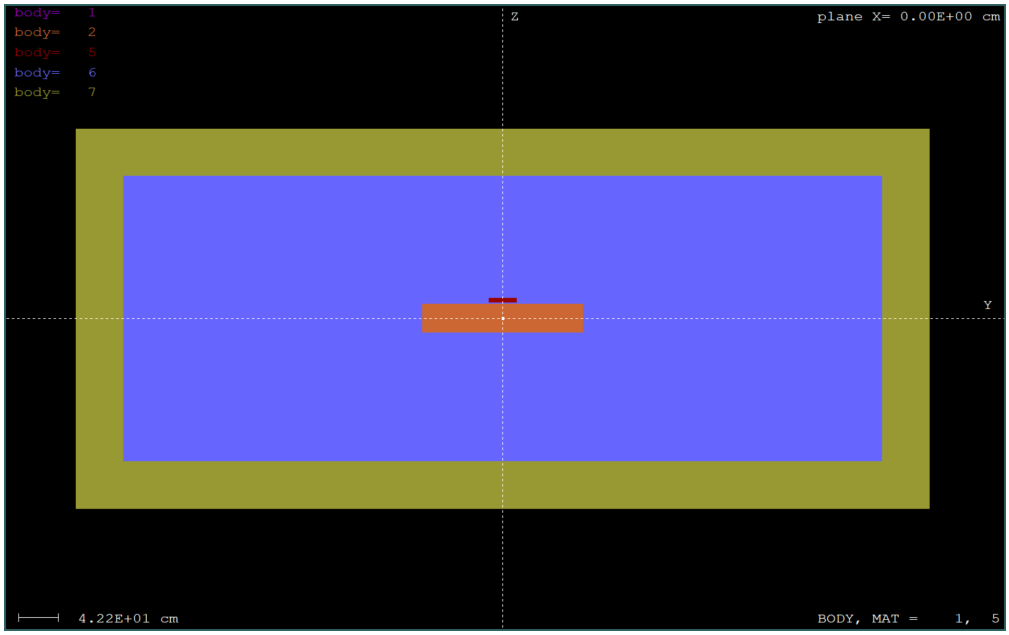


**Figure 4.8:** Frontal view (ZY) of the geometry with GVIEW 2D

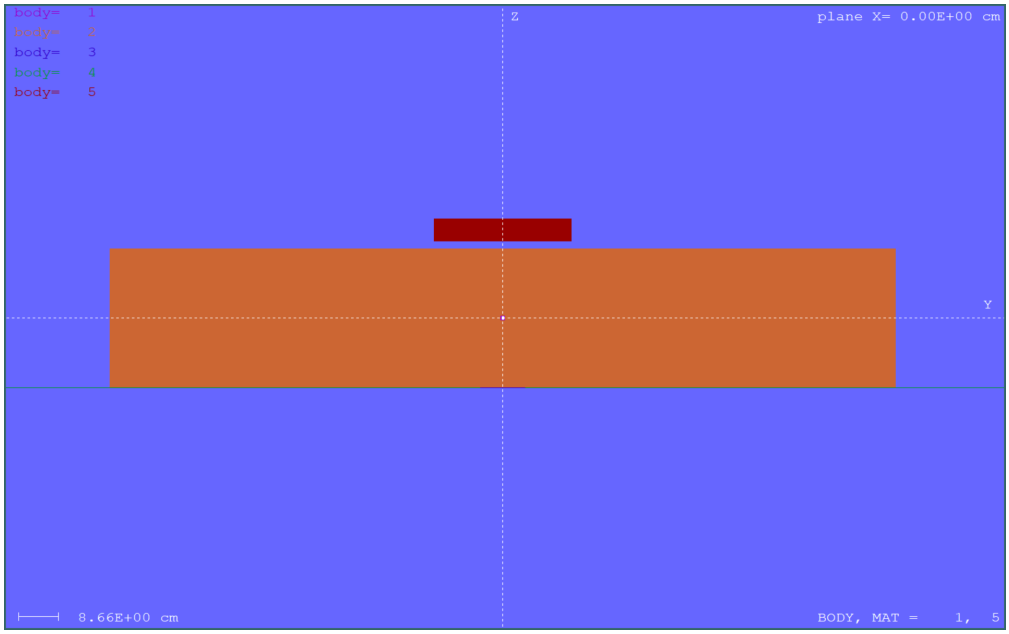


**Figure 4.9:** Frontal view (ZY) of the geometry with GVIEW 2D, focus on the cylinder with the table and silicon detector

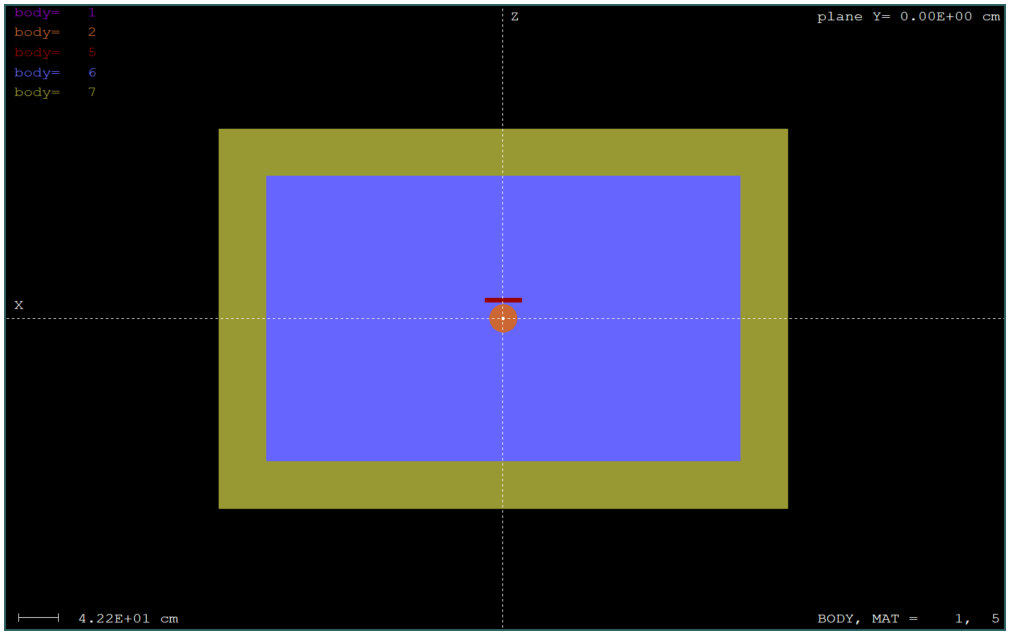


**Figure 4.10:** Lateral view (ZX) of the geometry with GVIEW 2D

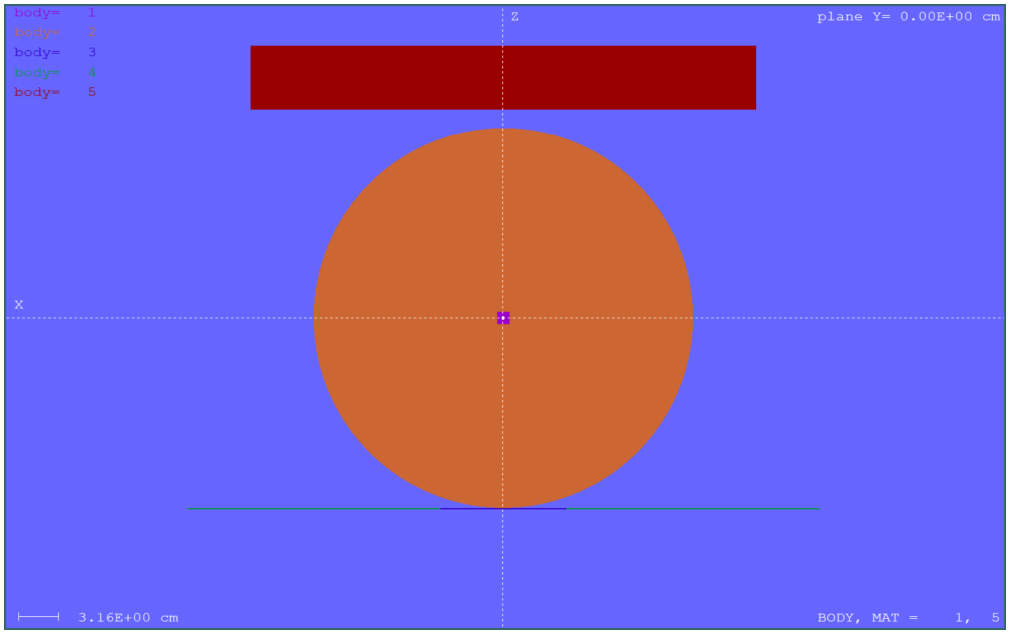


**Figure 4.11:** Lateral view (ZX) of the geometry with GVIEW 2D with focus on the table,silicon detector, box in the isocenter and cylinder

## 4.2 Problem definition, Voxelized geometry + quadric geometries

Regarding the case with the geometry composed of a mix of the two geometries, the base geometry is almost unchanged; the only difference is that the cylinder is replaced by a voxel geometry representing the body of an adult female, 163 cm tall and weighing 60 kg. This geometry accounts for the various organs and their positions within the human body. The voxels used in this geometry to represent the phantom are all sized 0.1775 cm x 0.1775 cm x 0.484 cm. The total number of voxels in the x, y, and z directions are 299, 137, and 348, respectively. All the various tissues and organs within the geometry were created using the guidelines provided in Publication 110 of the ICRP Annals [23]. The goals of this simulation are:

1. Total and mean dose deposited in the heart volume ( all ICRP voxels with index 33 and 55), simulating X-ray beam on the bottom (0°) with / without the table isocenter on the beam axis)

2. Depth dose distributions (beam axis) in the phantom for X-ray beam on the bottom (0°) and on the top (180°) of the table. Dose registered on the central

beam axis with voxel size of ICRP phantom (0.1775 cm, 0.1775 cm, 0.484 cm)).

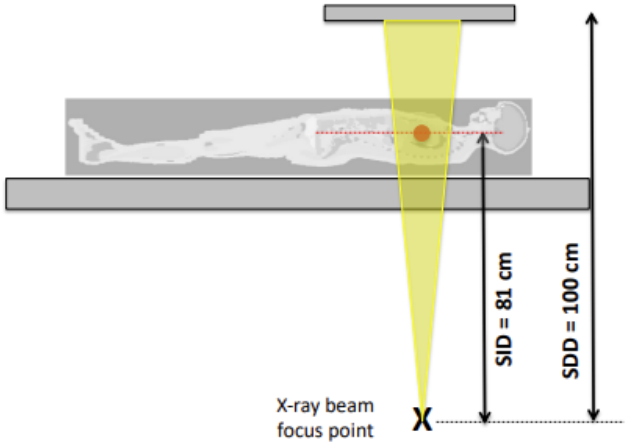


**Figure 4.12:** Schematic view of the geometry with both voxels and quadric surfaces [24]

### 4.2.1 Geometry definition, Voxels + Quadric Surfaces

Regarding the geometry involving the use of quadric surfaces and voxels, a similar geometry was created. The only difference is that by using a voxel-based geometry, this establishes the origin of our reference system, as explained previously. Therefore, the same elements as in the previous geometry were created, except for the cylinder, which is replaced by the phantom defined through voxels.

| Surface | Value (cm) |
|---|---|
| z | -365.78 |
| z | +534.22 |
| y | -187.84 |
| y | +212.16 |
| x | -273.46 |
| x | +326.54 |

**Table 4.9:** Concrete walls

| Surface | Value (cm) |
|---|---|
| z | -75.28 |
| z | +243.72 |
| y | -0.11 |
| y | +0 |
| x | +1.53 |
| x | +51.53 |

**Table 4.10:** Aluminum table

| Surface | Value (cm) |
|---|---|
| z | +124.228 |
| z | +134.228 |
| y | -0.11 |
| y | +0 |
| x | +18.608 |
| x | +28.608 |

**Table 4.11:** Source pointer

| Surface | Value (cm) |
|---|---|
| z | +109.1 |
| z | +149.1 |
| y | +28.79 |
| y | -33.79 |
| x | +8.608 |
| x | -38.608 |

**Table 4.12:** Detector

| Surface | Value (cm) |
|---|---|
| z | -315.78 |
| z | +484.22 |
| y | -137.84 |
| y | +162.16 |
| x | -223.46 |
| x | +276.54 |

**Table 4.13:** Air in the room

As can be seen from the definition of the quadric surfaces, the origin of our reference system has changed in this case. Specifically, as defined for the adult female phantom, the axis origin coincides with the tip of the left heel of the body. However, as mentioned previously, the geometry of this problem is nearly identical, with the only change being the replacement of the cylinder by the new phantom. This phantom was created using 53 different materials to represent the various regions of the body, including organs and tissues. The following table lists the materials and their composition by weight percentage of the various elements they contain.

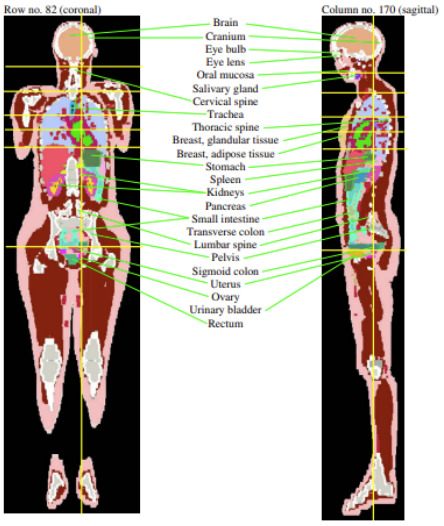


**Figure 4.13:** Coronal and sagittal images of the female phantom [23]

| Medium no. | | $H_1$ | $C_6$ | $N_7$ | $O_8$ | $Na_{11}$ | $Mg_{12}$ | $P_{15}$ | $S_{16}$ | $Cl_{17}$ | $K_{19}$ | $Ca_{20}$ | $Fe_{26}$ | $I_{53}$ | Density (g/cm) |
|---|---|---|---|---|---|---|---|---|---|---|---|---|---|---|---|
| 1 | Teeth | 2.2 | 9.5 | 2.9 | 42.1 | | 0.7 | 13.7 | | | | 28.9 | | | 2.750 |
| 2 | Mineral bone | 3.6 | 15.9 | 4.2 | 44.8 | 0.3 | 0.2 | 9.4 | 0.3 | | | 21.3 | | | 1.920 |
| 3 | Humeri, upper half, spongiosa | 8.5 | 28.8 | 2.6 | 49.8 | 0.2 | 0.1 | 3.3 | 0.4 | 0.2 | | 6.1 | | | 1.205 |
| 4 | Humeri, lower half, spongiosa | 9.7 | 43.9 | 1.7 | 38.1 | 0.2 | | 2.1 | 0.3 | 0.1 | | 3.9 | | | 1.108 |
| 5 | Lower arm bones, spongiosa | 9.7 | 43.9 | 1.7 | 38.1 | 0.2 | | 2.1 | 0.3 | 0.1 | | 3.9 | | | 1.108 |
| 6 | Hand bones, spongiosa | 9.7 | 43.9 | 1.7 | 38.1 | 0.2 | | 2.1 | 0.3 | 0.1 | | 3.9 | | | 1.108 |
| 7 | Clavicles, spongiosa | 9.1 | 34.8 | 2.4 | 45.7 | 0.2 | | 2.6 | 0.3 | 0.1 | | 4.8 | | | 1.151 |
| 8 | Cranium, spongiosa | 9.0 | 33.5 | 2.5 | 46.7 | 0.2 | | 2.6 | 0.3 | 0.2 | 0.1 | 4.9 | | | 1.157 |
| 9 | Femora, upper half, spongiosa | 9.4 | 38.5 | 2.2 | 43.0 | 0.2 | | 2.2 | 0.3 | 0.1 | | 4.1 | | | 1.124 |
| 10 | Femora, lower half, spongiosa | 9.7 | 43.9 | 1.7 | 38.1 | 0.2 | | 2.1 | 0.3 | 0.1 | | 3.9 | | | 1.108 |
| 11 | Lower leg bones, spongiosa | 9.7 | 43.9 | 1.7 | 38.1 | 0.2 | | 2.1 | 0.3 | 0.1 | | 3.9 | | | 1.108 |
| 12 | Foot bones, spongiosa | 9.7 | 43.9 | 1.7 | 38.1 | 0.2 | | 2.1 | 0.3 | 0.1 | | 3.9 | | | 1.108 |
| 13 | Mandible, spongiosa | 8.3 | 26.6 | 2.7 | 51.1 | 0.3 | 0.1 | 3.6 | 0.4 | 0.2 | | 6.7 | | | 1.228 |
| 14 | Pelvis, spongiosa | 9.4 | 36.0 | 2.5 | 45.4 | 0.2 | | 2.1 | 0.3 | 0.2 | 0.1 | 3.8 | | | 1.123 |
| 15 | Ribs, spongiosa | 8.9 | 29.2 | 2.9 | 50.7 | 0.2 | | 2.6 | 0.4 | 0.2 | 0.1 | 4.8 | | | 1.165 |
| 16 | Scapulae, spongiosa | 8.7 | 30.9 | 2.6 | 48.3 | 0.2 | 0.1 | 3.0 | 0.4 | 0.2 | | 5.6 | | | 1.183 |
| 17 | Cervical spine, spongiosa | 10.3 | 40.0 | 2.7 | 44.4 | 0.1 | | 0.7 | 0.2 | 0.2 | 0.1 | 1.2 | 0.1 | | 1.050 |
| 18 | Thoracic spine, spongiosa | 9.9 | 37.6 | 2.7 | 45.9 | 0.1 | | 1.2 | 0.2 | 0.2 | 0.1 | 2.0 | 0.1 | | 1.074 |
| 19 | Lumbar spine, spongiosa | 9.5 | 34.0 | 2.8 | 48.0 | 0.1 | | 1.8 | 0.3 | 0.2 | 0.1 | 3.2 | | | 1.112 |
| 20 | Sacrum, spongiosa | 10.5 | 41.9 | 2.7 | 43.2 | 0.1 | | 0.4 | 0.2 | 0.2 | 0.1 | 0.6 | 0.1 | | 1.031 |
| 21 | Sternum, spongiosa | 10.4 | 40.9 | 2.7 | 43.8 | 0.1 | | 0.6 | 0.2 | 0.2 | 0.1 | 0.9 | 0.1 | | 1.041 |
| 22 | Humeri and femora, upper halves, medullary cavity | 11.5 | 63.6 | 0.7 | 23.9 | 0.1 | | | 0.1 | 0.1 | | | | | 0.980 |
| 23 | Humeri and femora, lower halves, medullary cavity | 11.5 | 63.6 | 0.7 | 23.9 | 0.1 | | | 0.1 | 0.1 | | | | | 0.980 |
| 24 | Lower arm bones, medullary cavity | 11.5 | 63.6 | 0.7 | 23.9 | 0.1 | | | 0.1 | 0.1 | | | | | 0.980 |
| 25 | Lower leg bones, medullary cavity | 11.5 | 63.6 | 0.7 | 23.9 | 0.1 | | | 0.1 | 0.1 | | | | | 0.980 |
| 26 | Cartilage | 9.6 | 9.9 | 2.2 | 74.4 | 0.5 | | 2.2 | 0.9 | 0.3 | | | | | 1.100 |
| 27 | Skin | 10.0 | 19.9 | 4.2 | 65.0 | 0.2 | | 0.1 | 0.2 | 0.3 | 0.1 | | | | 1.090 |
| 28 | Blood | 10.2 | 11.0 | 3.3 | 74.5 | 0.1 | | 0.1 | 0.2 | 0.3 | 0.2 | | 0.1 | | 1.060 |
| 29 | Muscle tissue | 10.2 | 14.2 | 3.4 | 71.1 | 0.1 | | 0.2 | 0.3 | 0.1 | 0.4 | | | | 1.050 |
| 30 | Liver | 10.2 | 13.0 | 3.1 | 72.5 | 0.2 | | 0.2 | 0.3 | 0.2 | 0.3 | | | | 1.050 |
| 31 | Pancreas | 10.5 | 15.5 | 2.5 | 70.6 | 0.2 | | 0.2 | 0.1 | 0.2 | 0.2 | | | | 1.050 |
| 32 | Brain | 10.7 | 14.3 | 2.3 | 71.3 | 0.2 | | 0.4 | 0.2 | 0.3 | 0.3 | | | | 1.050 |
| 33 | Heart | 10.4 | 13.8 | 2.9 | 71.9 | 0.1 | | 0.2 | 0.2 | 0.2 | 0.3 | | | | 1.050 |
| 34 | Eyes | 9.7 | 18.1 | 5.3 | 66.3 | 0.1 | | 0.1 | 0.3 | 0.1 | | | | | 1.050 |
| 35 | Kidneys | 10.3 | 12.4 | 3.1 | 73.1 | 0.2 | | 0.2 | 0.2 | 0.2 | 0.2 | 0.1 | | | 1.050 |
| 36 | Stomach | 10.5 | 11.4 | 2.5 | 75.0 | 0.1 | | 0.1 | 0.1 | 0.2 | 0.1 | | | | 1.040 |
| 37 | Small intestine | 10.5 | 11.3 | 2.6 | 75.0 | 0.1 | | 0.1 | 0.1 | 0.2 | 0.1 | | | | 1.040 |
| 38 | Large intestine | 10.5 | 11.3 | 2.6 | 75.0 | 0.1 | | 0.1 | 0.1 | 0.2 | 0.1 | | | | 1.040 |
| 39 | Spleen | 10.2 | 11.1 | 3.3 | 74.3 | 0.1 | | 0.2 | 0.2 | 0.3 | 0.2 | | 0.1 | | 1.040 |
| 40 | Thyroid | 10.4 | 11.7 | 2.6 | 74.5 | 0.2 | | 0.1 | 0.1 | 0.2 | 0.1 | | | 0.1 | 1.040 |
| 41 | Urinary bladder | 10.5 | 9.6 | 2.6 | 76.1 | 0.2 | | 0.2 | 0.2 | 0.3 | 0.3 | | | | 1.040 |
| 42 | Testes | 10.6 | 10.0 | 2.1 | 76.4 | 0.2 | | 0.1 | 0.2 | 0.2 | 0.2 | | | | 1.040 |
| 43 | Adrenals | 10.4 | 22.1 | 2.8 | 63.7 | 0.1 | | 0.2 | 0.3 | 0.2 | 0.2 | | | | 1.030 |
| 44 | Oesophagus | 10.4 | 21.3 | 2.9 | 64.4 | 0.1 | | 0.2 | 0.3 | 0.2 | 0.2 | | | | 1.030 |
| 45 | Gall bladder, pituitary gland, trachea, thymus, tonsils, ureters | 10.4 | 23.1 | 2.8 | 62.7 | 0.1 | | 0.2 | 0.3 | 0.2 | 0.2 | | | | 1.030 |
| 46 | Prostate | 10.4 | 23.1 | 2.8 | 62.7 | 0.1 | | 0.2 | 0.3 | 0.2 | 0.2 | | | | 1.030 |
| 47 | Lymph | 10.8 | 4.2 | 1.1 | 83.1 | 0.3 | | | 0.1 | 0.4 | | | | | 1.030 |
| 48 | Breast (mammary gland) | 11.2 | 51.6 | 1.1 | 35.8 | 0.1 | | | 0.1 | 0.1 | | | | | 1.020 |
| 49 | Adipose tissue | 11.4 | 58.8 | 0.8 | 28.7 | 0.1 | | | 0.1 | 0.1 | | | | | 0.950 |
| 50 | Lung tissue (compressed lungs) | 10.3 | 10.7 | 3.2 | 74.6 | 0.2 | | 0.2 | 0.3 | 0.3 | 0.2 | | | | 0.382 |
| 51 | Gastro-intestinal tract – contents* | 10.0 | 22.2 | 2.2 | 64.4 | 0.1 | | 0.2 | 0.3 | 0.1 | 0.4 | 0.1 | | | 1.040 |
| 52 | Urine | 10.7 | 0.3 | 1.0 | 87.3 | 0.4 | | 0.1 | | | 0.2 | | | | 1.040 |
| 53 | Air | | | 80.0 | 20.0 | | | | | | | | | | 0.001 |

**Figure 4.14:** List of materials and their compositions used to define the female adult phantom [23]

# Chapter 5

# Results and conclusions

In this chapter it will be exposed and showed all the results obtained by running the several simulations for the different scenarios. All the simulations have been run by using $10^9$ histories, in order to have low values on the uncertainty of our variable of interest.

## 5.1 Results, Quadric Surfaces

### 5.1.1 Air Kerma

As explained in the previous chapter, the first quantity to be calculated is the air kerma in a 1 $cm^3$ box located 10 cm away from the X-ray source on the beam axis. This parameter has been evaluated by means of the tally **energy deposition**, a particular tally defined in the PENELOPE/penEasy program. This tally allows for the computation of the energy deposited by the photons, in our case, inside the region of interest. The unit of measurement of this output is eV/history, so further calculations must be done to get the proper unit of measure. The value computed inside the small box was:

$$\varepsilon_{\text{air}} = 1.74 \pm 0.014 \ \frac{eV}{history} \tag{5.1}$$

In order to get the air kerma, we need to divide it by the mass of air inside the box and convert the energy in joules to get the proper unit of measure. Remembering that 1 eV is equal to $1.6 \cdot 10^{-19}$ J, we can write:

$$\epsilon_{air} = \frac{\varepsilon_{air} \cdot 1.6 \cdot 10^{-19}}{m_{air}} = \frac{1.74 \cdot 1.6 \cdot 10^{-19}}{10^{-3}} = 2.78 \cdot 10^{-16} \ \frac{Gy}{history} \tag{5.2}$$

The value obtained using PENELOPE/penEasy matches the one obtained by Professor H. Brkic, who used the MCNP program to perform the Monte Carlo

**Table 5.1:** Kerma calculations (air volume = 1 $cm^3$, 10 cm after focus point) of others codes

| **Method** | **Value (Gy/history)** |
|---|---|
| Geant4/GATE | $2.87 \times 10^{-13}$ |
| MCNP | $7.59 \times 10^{-19}$ |
| MCNP | $4.00 \times 10^{-16}$ |
| MCNP | $2.39 \times 10^{-13}$ |
| MCNP | $2.94 \times 10^{-13}$ |
| PHITS | $1.41 \times 10^{-13}$ |
| MCGPU-IR | $2.17 \times 10^{-13}$ |

simulations. Discrepancies between the results could be result of different source definitions and therefore, for any comparison dose results should be normalised by using these value.

### 5.1.2 X-ray energy spectrum

The X-ray spectrum has been computed by means of the tally **fluence track length**. The only problem is that PENELOPE is not able to compute the volume of a body defined through quadric surfaces [21]. Indeed, instead of having as output the fluence spectrum, which is supposed to have as unit of measure $\frac{\text{counts}}{\text{eV}\cdot\text{cm}^2}$, it returns the fluence spectrum multiplied by the volume of the body where it is computed, that is, in our case, the volume of the box located at the isocenter of the phantom. Moreover, in order to obtain the correct result, it is needed to multiply this quantity to the energy of each bin the energy range has been split in, in our case the energy of every bin is of 1427 eV.

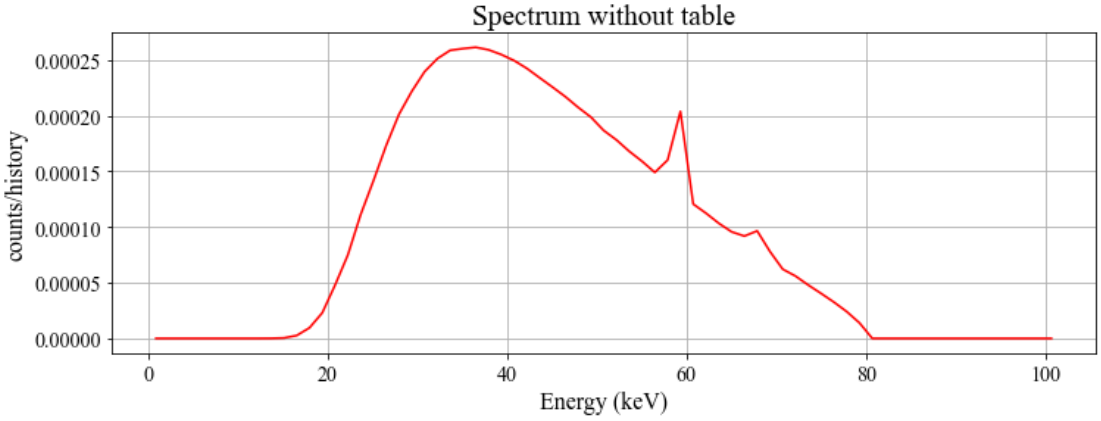


**Figure 5.1:** X-ray spectrum without the Aluminum table

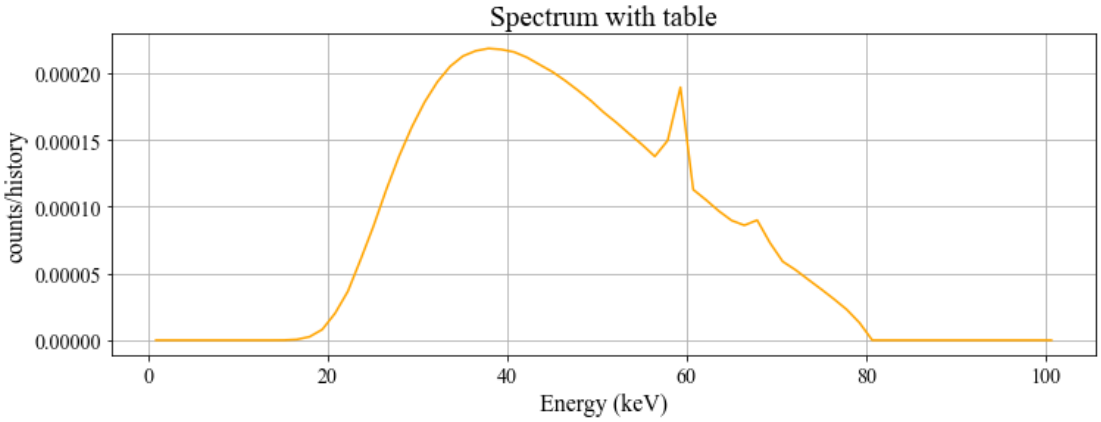


**Figure 5.2:** X-ray spectrum with the Aluminum table

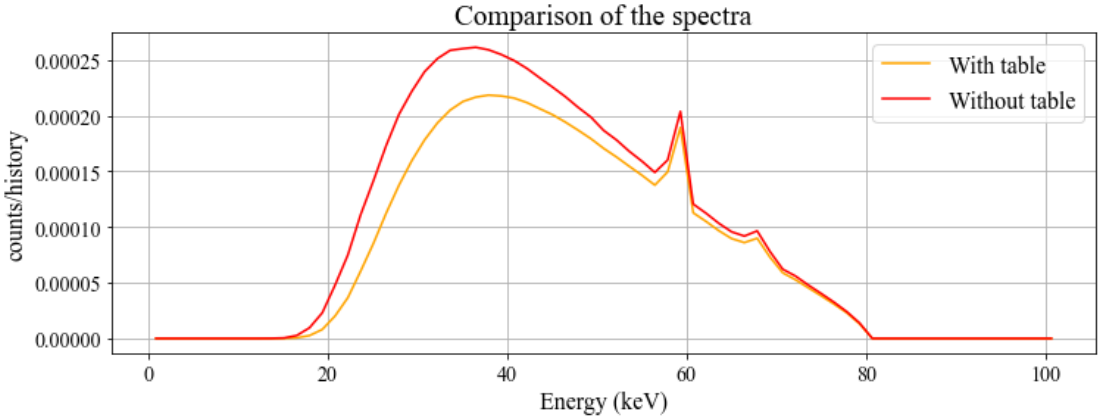


**Figure 5.3:** Comparison of the X-ray spectra

The trends of the energy spectrum for both cases, with and without the aluminum table, are very similar, and both follow the trend of the emission spectrum used as input for the simulations. As can be seen from the comparison between the two spectra, the presence of the aluminum table leads to greater attenuation of the photons, resulting in a reduction in the number of photons that reach the isocenter within the cylinder, having a lower number of counts. Since the numerical data of the results obtained by the other participants in this project are not available, it is only possible to assess the correctness of the results by looking at the trends of the energy spectra obtained by the other participants.

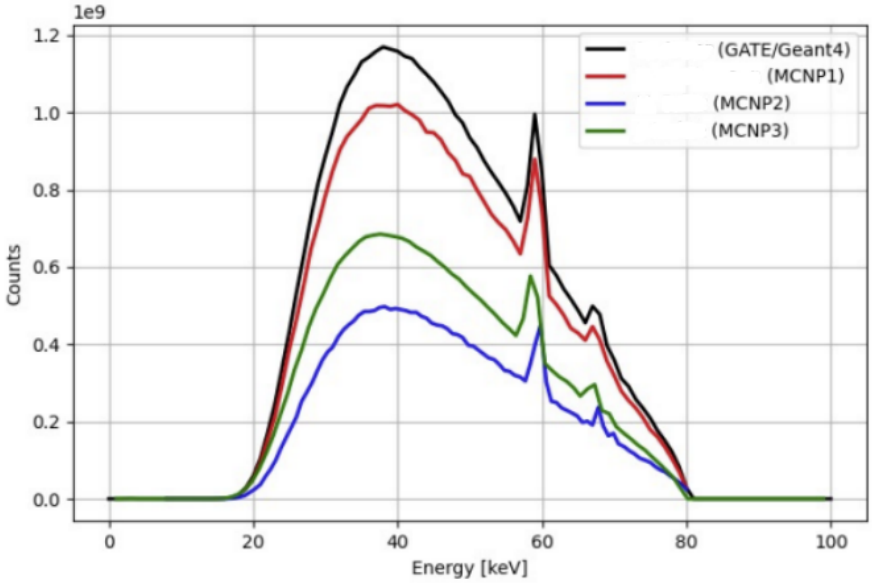


**Figure 5.4:** X-ray spectra with the table computed from some of the other participants[25]

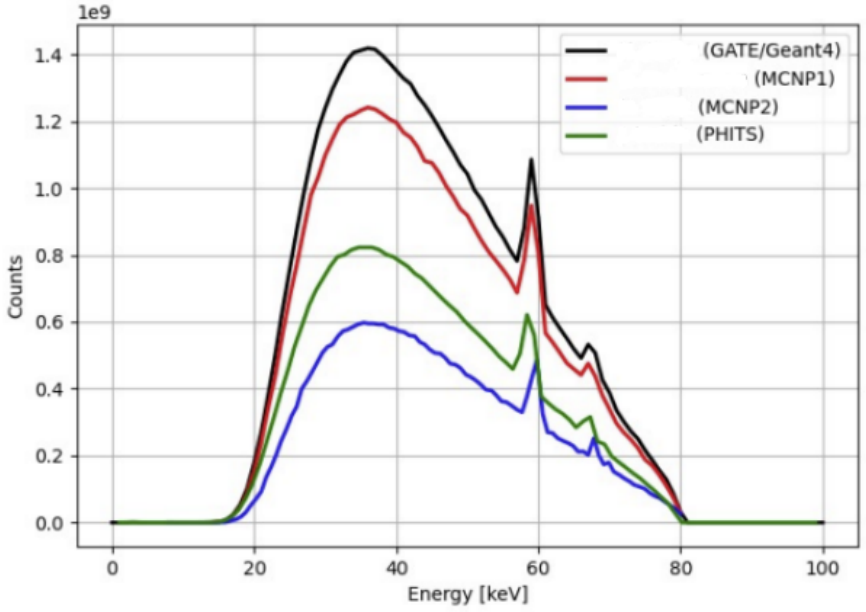


**Figure 5.5:** X-ray spectra without the table computed from some of the other participants [25]

The energy spectra of the other participants have all been normalized with

respect to air kerma, reason for which there are differences on the magnitude of the results. What is noticeable, however, is that the behavior of the spectra is almost identical, disregarding the numerical value. All the results show peaks in the same energy ranges, and they all demonstrate the attenuation effect introduced by the presence of the aluminum table.

### 5.1.3 Dose and fluence

In order to compute the dose, the same tally **energy deposition** has been used. The dose delivered in the box was calculated for both configurations, to evaluate the effect that the aluminum table has on this variable. Both the simulations have been run by using air as material for the phantom.

| | Energy (eV/history) | $\sigma$ (%) |
|---|---|---|
| With table | $1.95 \cdot 10^{-2}$ | 7.96 |
| Without table | $2.52 \cdot 10^{-2}$ | 6.95 |

**Table 5.2:** Energy deposition in the box with corresponding uncertainty

To obtain the dose, expressed in Gy, we apply the same procedure used to calculate the air kerma.

| | Dose (Gy/history) |
|---|---|
| With table | $3.12 \cdot 10^{-16} \pm 0.25 \cdot 10^{-16}$ |
| Without table | $4.03 \cdot 10^{-16} \pm 0.32 \cdot 10^{-16}$ |

**Table 5.3:** Dose in the box

Of particular interest is the uncertainty regarding the deposited energy. This value is significant despite the high number of simulated histories. In Monte Carlo methods, uncertainty decreases as the number of simulated particles **N** increases, as follows [26]:

$$\sigma \propto \frac{1}{\sqrt{N}} \tag{5.3}$$

In this case, because the box is relatively far from the source, the number of photons interacting with it is further reduced by scattering or absorption. Thus, achieving very low uncertainty would require increasing the number of simulated particles, leading to higher computational cost and time for the simulation. Regarding the fluence, it has been computed by using the output of the tally used

to compute the spectrum. In particular as discussed before, this tally gives the fluence spectrum multiplied by the volume of the region where we are computing it, so:

$$\text{tally fluence track length} \xrightarrow{\text{output}} V\frac{d\Phi}{dE} \tag{5.4}$$

The unit of measure of this output are $\frac{cm}{eV \cdot history}$. So to obtain the total value of the fluence for the box in the isocenter we need to divide by the volume of the box and integrate over the energy spectrum as it follows:

$$\Phi = \frac{1}{V_{box}} \int_{E_{\min}}^{E_{\max}} [V\frac{d\Phi}{dE}]\, dE \tag{5.5}$$

The fluence values are:

| | Fluence $\left(\frac{1}{\text{cm}^2 \cdot \text{history}}\right)$ |
|---|---|
| With table | $5.49 \cdot 10^{-3}$ |
| Without table | $6.55 \cdot 10^{-3}$ |

**Table 5.4:** Fluence in the box

Regarding these values, the calculated figures from other participants have not yet been provided, so a comparison cannot be made.

### 5.1.4 Depth dose distribution

The objective of this simulation is to analyze the dose distribution within the PMMA cylinder, specifically examining how this distribution varies in the presence of the table. The tally used to compute it was **spatial dose distribution**, this tally allows to calculate the spatial dose distribution along the several spatial coordinates. In this case we compute the distribution along the z-coordinate, along the whole height of the cylinder, so 30 cm. This length has been split into 300 bins having bins of 0.1 cm.

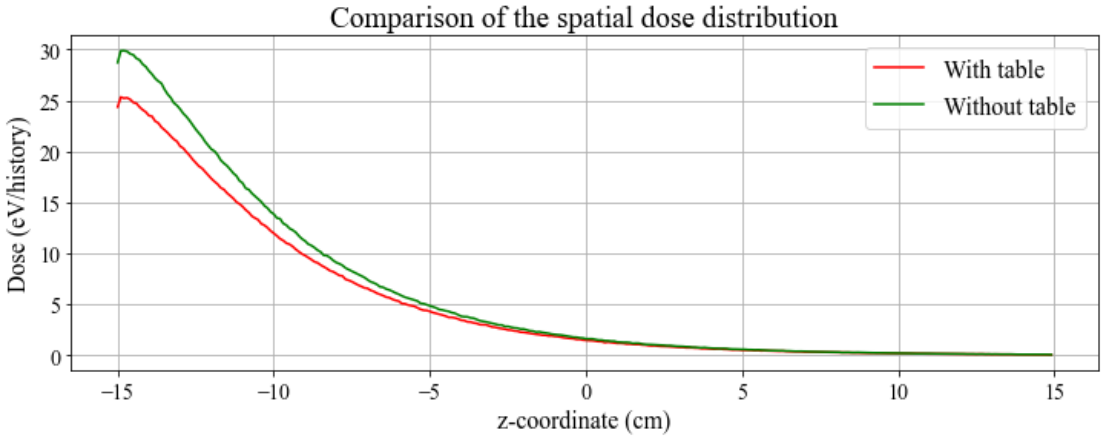


**Figure 5.6:** Comparison between the spatial dose distribution

As can be seen from the graphs, the dose distribution within the cylinder shows a peak in the initial region. This is due to the fact that, in defining the tally for the spatial dose distribution, the first bin includes part of the domain with air and part of the domain with PMMA. After the entrance region, the trend continues following an exponential pattern, in line with the explanations in the section on photon interactions with matter. Obviously, as previously highlighted, the reduced dose values in the presence of the aluminum table are due to the additional attenuation caused by the table itself. For the spatial dose distribution, in the case with the aluminum table, it was possible to compare it with the distribution obtained using the MCGPU program, as the numerical data of the obtained results were provided.

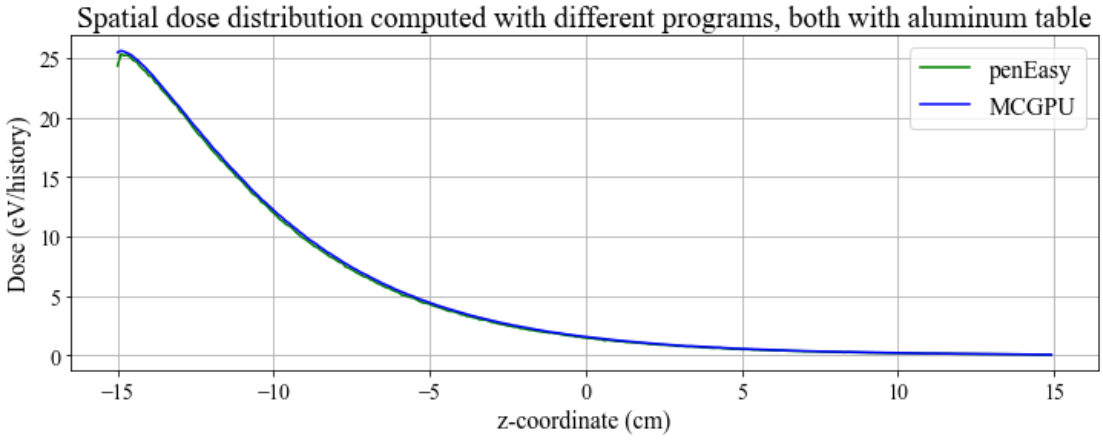


**Figure 5.7:** Spatial dose distributions with aluminum table computed with different sofwtare

Both the simulation done using penEasy and the one done with MCGPU produced the same result. Therefore, it can be confirmed that the simulations were set up correctly.

## 5.2 Results, voxelized + quadric Surfaces

### 5.2.1 Total and mean dose deposited in the heart volume

The heart in voxel-based geometry is identified by all voxels with ID numbers 33 and 55, corresponding to the heart and blood, respectively. To calculate the total dose, it is necessary to determine the mass of both within the phantom. For this, the number of voxels with the relevant ID numbers was calculated, and, once this count was obtained, it was possible to calculate the volume and, consequently, the total mass. Within the geometry, there are 15,614 voxels with ID number 33 and 22,891 with ID number 55. This allows us to calculate the mass as follows:

$$V_{voxels} = L_x \cdot L_y \cdot L_z \tag{5.6}$$

Where $L_x$, $L_y$, and $L_z$ represent the lengths of the sides of the voxel, they are 0.1775 cm, 0.1775 cm, and 0.484 cm respectively. Thus, the volume of a single voxel is:

$$V_{\text{voxel}} = L_x \cdot L_y \cdot L_z = 0.1775\,\text{cm} \cdot 0.1775\,\text{cm} \cdot 0.484\,\text{cm}$$

Calculating this gives:

$$V_{\text{voxel}} = 0.01524\,\text{cm}^3$$

The total volume of the heart (ID number of 33) and of the blood (ID number of 55) are :

$$V_{heart} = V_{\text{voxel}} \cdot N_{33} = 0.01524 \cdot 15614 = 238.10\ \text{cm}^3$$

$$V_{blood} = V_{\text{voxel}} \cdot N_{55} = 0.01524 \cdot 22981 = 350.23\ \text{cm}^3$$

The mass density of the two materials are $\rho_{\text{heart}} = 1.05\,\text{g/cm}^3$ and $\rho_{\text{blood}} = 1.06\,\text{g/cm}^3$, so the total mass of the two materials is computed as:

$$m_{heart} = V_{\text{heart}} \cdot \rho_{\text{heart}} = 238.10 \cdot 1.05 = 250\ \text{g}$$

$$m_{blood} = V_{\text{blood}} \cdot \rho_{\text{blood}} = 350.23 \cdot 1.06 = 371.24\ \text{g}$$

The energy deposited within the two materials was calculated using the same tally as before, and the resulting values are shown in the table.

| | Energy (eV/history) |
|---|---|
| Heart | 919.18 ±0.35 |
| Blood | 1518.92 ±0.47 |

**Table 5.5:** Energy deposited in both heart and blood with aluminum table

| | Energy (eV/history) |
|---|---|
| Heart | 1041.17 ±0.37 |
| Blood | 1715.65 ±0.49 |

**Table 5.6:** Energy deposited in both heart and blood without aluminum table

To calculate the total dose, we add the doses in the respective materials, converting them to the appropriate units as done previously. However, special attention is required now since we have two results with two different uncertainties, which are independent of each other. To calculate the uncertainty of the final result, obtained by summing the two doses, the following formula is used [27]:

$$\delta S = \sqrt{(\delta A)^2 + (\delta B)^2} \tag{5.7}$$

This formula tells us that the uncertainty in the final result is given by the square root of the sum of the squared uncertainties

| | Dose (Gy/history) |
|---|---|
| Heart | $5.88 \times 10^{-16} \pm 2.24 \times 10^{-19}$ |
| Blood | $6.55 \times 10^{-16} \pm 2.03 \times 10^{-19}$ |

**Table 5.7:** Dose in both heart and blood with aluminum table

| | Dose(Gy/history) |
|---|---|
| Heart | $6.66 \times 10^{-16} \pm 2.36 \times 10^{-19}$ |
| Blood | $7.39 \times 10^{-16} \pm 2.11 \times 10^{-19}$ |

**Table 5.8:** Dose in both heart and blood without aluminum table

At this point, it is possible to calculate the total dose in the volume of the heart for both configurations, with and without the aluminum table.

| Condition | Dose (Gy/history) |
|---|---|
| With table | $1.24 \times 10^{-15} \pm 3.02 \times 10^{-19}$ |
| Without table | $1.20 \times 10^{-15} \pm 3.17 \times 10^{-19}$ |

**Table 5.9:** Total dose in the heart volume

As for the mean absorbed dose in the volume of the heart, to calculate it we start from the general definition of this quantity defined in the first chapter:

$$\overline{D_{\mathrm{T}}} = \frac{\int D(x,y,z)\,\rho(x,y,z)\,dV}{\int \rho(x,y,z)\,dV} \tag{5.8}$$

This formula needs to be adapted to our situation. Since the phantom is made up of small squares, the use of the integral is impossible, as a continuous function of the dose along the materials of interest is not available. Therefore, this formula, while correct, is adapted to our situation as follows:

$$\overline{D_{\mathrm{T}}} = \frac{\sum_i D_i\,\rho_i\,\Delta V_i}{\sum_i \rho_i\,\Delta V_i} \tag{5.9}$$

It is evident that, given the constant density of the materials and the same volume of the voxels, the equation above becomes:

$$\overline{D_{\mathrm{T}}} = \frac{D_{heart} \cdot m_{heart} + D_{blood} \cdot m_{blood}}{m_{heart} + m_{blood}} \tag{5.10}$$

After performing the calculations, using as input the values calculated previously, the mean absorbed dose in the volume of the heart is:

| | $\overline{D_{\mathrm{T}}}\ (Gy/history)$ |
|---|---|
| With table | $6.28 \times 10^{-16} \pm 3.02 \times 10^{-19}$ |
| Without table | $7.10 \times 10^{-16} \pm 3.17 \times 10^{-19}$ |

**Table 5.10:** Mean absorbed dose in the heart volume

It was possible to make a comparison with the values obtained, always for the same quantity, using other codes for the case with the aluminum table. As can be observed from the following table, the value of the mean absorbed dose in the heart is very close to that obtained using the GATE and MCNP software.

| | $\overline{D_T}$ (Gy/history) |
|---|---|
| PENELOPE/penEasy | $6.28 \times 10^{-16}$ |
| GATE | $6.71 \times 10^{-16}$ |
| MCNP | $4.09 \times 10^{-16}$ |

**Table 5.11:** Mean absorbed dose in the heart volume results from other codes.

### 5.2.2 Depth dose distributions

Like in the previous case with the quadric surfaces, we also want to see what the dose profile looks like within the patient for the voxels. To calculate this variable, the tally **VoxelDoseDistribution** was used. This tally operates in the same way as the one used in the case of quadric surfaces; the only difference is that the coordinates of the voxels along which the dose distribution is to be reproduced must be specified.

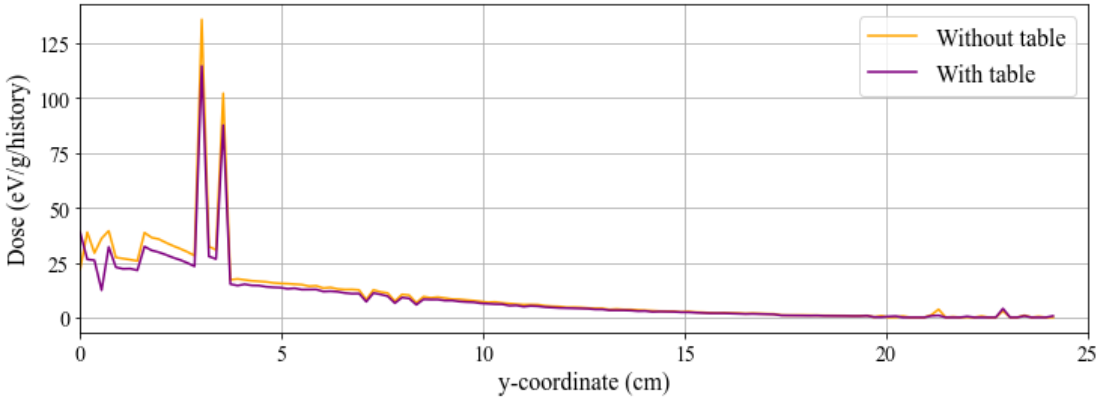


**Figure 5.8:** Spatial dose distribution for both the configuration along the central beam axis

Unlike the previous situation, where we had a cylinder made of a single material, in this case, having different materials in the various areas of the phantom, the distribution no longer follows an exponential trend. Furthermore, we observe peaks; this is due to the fact that the materials have different densities, which consequently results in different absorbed doses. In our case, the peaks are due to the presence of the ribs, primarily composed of spongiosa bone material. In the next graph, a comparison is shown between the results obtained using the PenEasy and MCGPU software concerning the dose distribution in the case without the table. Both simulations exhibit nearly identical values and trends, except in the initial region. A possible reason for this discrepancy could be slight differences in the geometry and position of the photon source. Both simulations display peaks in the same regions where the previously mentioned materials are located, and the

dose decreases to values close to zero.

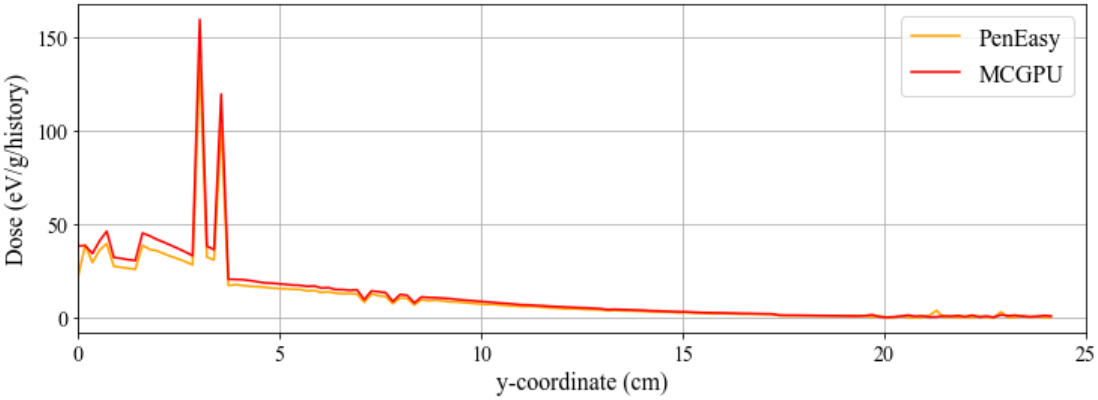


**Figure 5.9:** Comparison between dose distribution without aluminum table with MCGPU and PenEasy software

Significant differences between the two results were observed in the peak regions. Specifically, in the two peaks, the error of the simulation performed using penEasy compared to that with MCGPU was 39.20% and 36.27%, respectively.

### 5.2.3 Conclusions

Monte Carlo simulations have produced in-depth data on dose distribution in interventional radiology, particularly illustrating the effect of photon transport configurations and setup on dose and fluence parameters. Key findings indicate that different configurations and materials contribute significantly to dose variation, highlighting the potential for optimizing interventional procedures to improve patient safety. Furthermore, some values obtained from these simulations will be compared with analytical values provided by other participants, allowing further validation and benchmarking of the results. This comparison will strengthen the reliability of the simulations by confirming their alignment with the analytical models. The approach, which focused exclusively on photon transport and excluded contributions from electrons and positrons, simplified the model while maintaining accuracy.In order to simulate only photon transport, a high absorption energy threshold was set for electrons and positrons. This way, once they are generated by possible photon interactions with matter, they are instantly absorbed. This methodology supports the goal of accurately estimating radiation dose in a controlled but representative setting, ensuring that the results are applicable to real-world clinical scenarios. Overall, the simulation results highlight the utility of Monte Carlo methods in radiology to evaluate dose impacts and improve procedural parameters. This information, combined with further comparison to analytical benchmarks, can guide safer and more effective radiology practices.

# Bibliography


[1] Stephen Balter, John W Hopewell, Donald L Miller, Louis K Wagner, and Michael J Zelefsky. «Fluoroscopically guided interventional procedures: a review of radiation effects on patients' skin and hair». In: *Radiology* 254.2 (2010), pp. 326–341 (cit. on pp. 3, 4, 14).

[2] Radiological Protection. «ICRP publication 103». In: *Ann ICRP* 37.2.4 (2007), p. 2 (cit. on pp. 4–9).

[3] John R Lamarsh, Anthony John Baratta, et al. *Introduction to nuclear engineering*. Vol. 3. Prentice hall Upper Saddle River, NJ, 2001 (cit. on pp. 7, 8).

[4] Dennise Magill, Nhan James Huu Ngo, Marc A Felice, and Mel Mupparapu. «Kerma area product (KAP) and scatter measurements for intraoral X-ray machines using three different types of round collimation compared with rectangular beam limiter». In: *Dentomaxillofacial Radiology* 48.2 (2019), p. 20180183 (cit. on p. 9).

[5] Walter Huda. «Kerma-area product in diagnostic radiology». In: *American Journal of Roentgenology* 203.6 (2014), W565–W569 (cit. on p. 9).

[6] European Commission. «Medical radiation exposure of the European population». In: *Radiat. Protect.* 181 (2014) (cit. on pp. 10, 11, 13).

[7] B Wall, D Hart, H Mol, A Lecluyse, A Aroua, P Trueb, et al. «European guidance on estimating population doses from medical X-ray procedures». In: *Luxembourg: Publications Office* (2008) (cit. on pp. 10, 12).

[8] International Atomic Energy Agency AEA. *Radiation protection in fluoroscopy*. URL: `https://www.iaea.org/resources/rpop/health-professionals/radiology/fluoroscopy` (cit. on p. 13).

[9] International Atomic Energy Agency AEA. *Preventing unnecessary exposure in fluoroscopy*. URL: `https://www.iaea.org/resources/rpop/health-professionals/radiology/fluoroscopy` (cit. on p. 13).

[10] Philips. *Philips Launches New Azurion Neuro Biplane System at ECR 2024*. Accessed: 2024-06-20. 2024. URL: https://www.philips.es/a-w/about/news/archive/standard/news/press/2024/20240227-philips-launches-new-azurion-neuro-biplane-system-at-ecr2024-to-speed-up-and-improve-minimally-invasive-diagnosis-and-treatment-of-neurovascular-patients.html (cit. on p. 14).

[11] IAEA (Corporate Author) and IAEA (Corporate Editor). *Patient dose optimization in fluoroscopically guided interventional procedures*. International Atomic Energy Agency, 2010 (cit. on p. 15).

[12] MM Rehani, O Ciraj-Bjelac, E Vañó, DL Miller, S Walsh, BD Giordano, and J Persliden. «Radiological protection in fluoroscopically guided procedures performed outside the imaging department». In: *Annals of the ICRP* 40.6 (2010), pp. 1–102 (cit. on pp. 15, 16).

[13] *Circulation*. Accessed: 2024-06-20. 2007. URL: https://doi.org/10.1161/CIRCULATIONAHA.107.688101 (cit. on p. 16).

[14] Paul A Tipler and Gene Mosca. *Physics for scientists and engineers with modern physics*. Susan Finnemore Brennan, 2008 (cit. on p. 17).

[15] Claudio Canuto, Anita Tabacco, Claudio Canuto, and Anita Tabacco. «Calcolo differenziale». In: *Analisi matematica I* (2014), pp. 175–234 (cit. on p. 19).

[16] Francesc Salvat, José M Fernández-Varea, Josep Sempau, et al. «PENELOPE-2006: A code system for Monte Carlo simulation of electron and photon transport». In: *Workshop proceedings*. Vol. 4. 6222. Citeseer. 2006, p. 7 (cit. on pp. 19–21, 24, 25, 27–29).

[17] Dylan Y Breitkreutz, Michael D Weil, and Magdalena Bazalova-Carter. «External beam radiation therapy with kilovoltage x-rays». In: *Physica Medica* 79 (2020), pp. 103–112 (cit. on pp. 21, 23).

[18] ARPANSA. *Understanding Radiation: Ionising Radiation - X-ray*. 2024. URL: https://www.arpansa.gov.au/understanding-radiation/what-is-radiation/ionising-radiation/x-ray (cit. on p. 22).

[19] Patrick T McCarthy, Ronald G Reifenberger, and Timothy S Fisher. «Thermionic and photo-excited electron emission for energy-conversion processes». In: *Frontiers in Energy Research* 2 (2014), p. 54 (cit. on p. 22).

[20] Syed Naeem Ahmed. *Physics and engineering of radiation detection*. Academic Press, 2007 (cit. on p. 22).

[21] J. Sempau, A. Badal, and L. Brualla. «A PENELOPE-based system for the automated Monte Carlo simulation of clinacs and voxelized geometries—application to far-from-axis fields». In: *Med. Phys.* 38 (2011). Available at http://dx.doi.org/10.1118/1.3643029, pp. 5887–5895 (cit. on pp. 24, 30, 46).

[22] Philips Healthcare. *Philips FD20: Technical Manual*. Version 3. 2023 (cit. on p. 33).

[23] International Commission on Radiological Protection. *ICRP Publication 110: Adult Reference Computational Phantoms*. Annals of the ICRP, Volume 39, Issue 2. ICRP Publication 110 describes computational phantoms for adult reference male and female, based on tomographic data. Elsevier, 2009. ISBN: 978-0-7020-4186-0 (cit. on pp. 41, 43, 44).

[24] Philips. *Philips Allura FD20 (ICRP 110)*. 2023 (cit. on p. 42).

[25] EURADOS. *EURADOS2022_WG12_Task5Meeting*. 2022. URL: `inserisci%20qui%20l'URL` (cit. on p. 48).

[26] Daryoush Sheikh-Bagheri, Iwan Kawrakow, Blake Walters, and DWO Rogers. «Monte Carlo simulations: efficiency improvement techniques and statistical considerations». In: *Integrating new technologies into the clinic: Monte Carlo and image-guided radiation therapy, Proceedings of the 2006 AAPM Summer School. Madison, WI: Medical Physics Publishing* (2006), pp. 71–91 (cit. on p. 49).

[27] M Palmer. «Propagation of uncertainty through mathematical operations». In: *Massachusetts Institute of* (2003) (cit. on p. 53).